

# An Assessment of CFD/CSD Prediction State-of-the-Art Using the HART II International Workshop Data

Marilyn J. Smith\*  
Georgia Inst. of Tech.  
Atlanta, GA, USA

Joon W. Lim<sup>†</sup>  
US Army AFDD-1 (AMRDEC)  
Moffett Field, CA, USA

Berend G. van der Wall<sup>‡</sup>  
German Aerospace Center (DLR)  
Braunschweig, Germany

James D. Baeder<sup>§</sup>  
University of Maryland  
College Park, MD, USA

Robert T. Biedron<sup>¶</sup>  
NASA Langley Research Center  
Hampton, VA, USA

D. Douglas Boyd, Jr.<sup>||</sup>  
NASA Langley Research Center  
Hampton, VA, USA

Buvana Jayaraman\*\*  
Science & Technology Corp.  
Moffett Field, CA, USA

Sung N. Jung<sup>††</sup>  
Konkuk University  
Seoul, South Korea

Byung-Young Min<sup>‡‡</sup>  
Georgia Inst. of Tech.  
Atlanta, GA, USA

Over the past decade, there have been significant advancements in the accuracy of rotor aeroelastic simulations with the application of computational fluid dynamics methods coupled with computational structural dynamics codes (CFD/CSD). The HART II International Workshop database, which includes descent operating conditions with strong blade-vortex interactions (BVI), provides a unique opportunity to assess the ability of CFD/CSD to capture these physics. In addition to a baseline case with BVI, two additional cases with 3/rev higher harmonic blade root pitch control (HHC) are available for comparison. The collaboration during the workshop permits assessment of structured, unstructured, and hybrid overset CFD/CSD methods from across the globe on the dynamics, aerodynamics, and wake structure. Evaluation of the plethora of CFD/CSD methods indicate that the most important numerical variables associated with most accurately capturing BVI are a two-equation or detached eddy simulation (DES)-based turbulence model and a sufficiently small time step. An appropriate trade-off between grid fidelity and spatial accuracy schemes also appears to be important for capturing BVI on the advancing rotor disk. Overall, the CFD/CSD methods generally fall within the same accuracy; cost-effective hybrid Navier-Stokes/Lagrangian wake methods tend to correlate less accurately with experiment and have larger data scatter than the full CFD/CSD methods for most parameters evaluated. The importance of modeling the fuselage is observed, and other requirements are discussed.

---

\* corresponding author, Associate Professor, mari-lyn.smith@ae.gatech.edu

<sup>†</sup> Research Scientist, lim@merlin.arc.nasa.gov

<sup>‡</sup> Senior Scientist, berend.vanderwall@dlr.de

<sup>§</sup> Associate Professor, baeder@umd.edu

<sup>¶</sup> Senior Research Scientist, r.t.biedron@nasa.gov

<sup>||</sup> Senior Research Engineer, d.d.boyd@nasa.gov

<sup>\*\*</sup> Research Scientist, buvana.jayaraman@us.army.mil

<sup>††</sup> Professor, snjung@konkuk.ac.kr

<sup>‡‡</sup> Senior Research Scientist currently at the United Technologies Research Center, minb@utrc.utc.com  
Presented at the American Helicopter Society 68th Annual Forum, Ft. Worth, TX, May 1–3, 2012. This is a work of the U.S. Government and is not subject to copyright protection in the U.S.

---

This information product has been reviewed and approved for public release. The views expressed herein are those of the author and do not reflect the official policy or position of the Department of the Army, Department of Defense, or the U.S. Government. Reference herein to any specific commercial, private or public products, process, or service by trade name, trademark, manufacturer, or otherwise, does not constitute or imply its endorsement, recommendation, or favoring by the United States Government.

## NOMENCLATURE

$a_\infty$	speed of sound, m/s
$c$	airfoil chord, m
$C_m M^2$	section moment coefficient, $C_m M^2 = (dM_{c/4}/dy)/(\rho_\infty a_\infty^2 c^2/2)$
$C_n M^2$	section force coefficient, $C_n M^2 = (dL'/dy)/(\rho_\infty a_\infty^2 c/2)$
$C_T$	thrust coefficient, $C_T = T/(\rho_\infty \pi \Omega^2 R^4)$
$f, g$	function
$dL'/dy$	section lift, N/m
$dM_{c/4}/dy$	section moment, Nm/m
$M_h$	hover tip Mach number, $M_h = \Omega R/a_\infty$
$M_x$	rotor hub roll moment, Nm
$M_y$	rotor hub pitch moment, Nm
$M_\infty$	free-stream Mach number, $M_\infty = V_\infty/a_\infty$
$n$	integer
$N_b$	number of blades
$p_\infty$	static air pressure, kPa
$P$	rotor power, kW
$r$	Pearson product moment coefficient
$r_a$	non-dimensional root cut-out radius
$r_{tw}$	non-dimensional zero twist radius
$R$	rotor radius, m
$s$	standard deviation, variable units
$t$	time, s
$T$	thrust, N
$T_\infty$	air temperature, °C
$V_\infty$	air speed, m/s
$x, y, z$	chord, radial, normal coordinates, respectively, m
$x_{el}$	elastic deflection, m
$x_{hub}$	Hub center distance to nozzle, m
$y_{hub}$	Hub position above centerline, m
$\alpha$	angle of attack, degrees
$\alpha_S$	rotor shaft angle of attack, degrees
$\Delta\alpha_s$	wind tunnel interference angle, degrees
$\phi$	mode shape
$\Theta_C$	lateral cyclic pitch angle, degrees
$\Theta_S$	longitudinal cyclic pitch angle, degrees
$\Theta_{el}$	elastic twist angle, degrees
$\Theta_{tw}$	linear blade twist, degrees/R
$\Theta_{75}$	collective pitch angle at 0.75R, degrees
$\Theta_3$	HHC pitch angle at 3/rev, degrees
$\mu$	advance ratio, $\mu = V_\infty \cos\alpha_S/(\Omega R)$
$\rho_\infty$	air density, kg/m <sup>3</sup>
$\sigma$	rotor solidity, $\sigma = N_b c/(\pi R^2)$
$\psi$	azimuth, $\psi = \Omega t$ , degrees
$\psi_3$	phase of 3/rev HHC pitch angle, degrees
$\Omega$	rotor rotational frequency, radians/s
$\bar{\cdot}$	mean

## INTRODUCTION

During the past decade, an experimental data set developed via a significant international collaboration has been obtained and extensively studied. This data set, known as the HART II rotor data set, has provided a wealth of performance data (airloads and wake), as well as aeroacoustics data for the development of aeroelastic and aeroacoustic prediction methods. A subset of these data was opened to the public in 2005; and in conjunction with the release of these experimental data, a series of workshops (Ref. 1) have been held, first on a semi-annual and more recently on an annual basis. Active participants of the workshop have included researchers from the US government (AFDD, NASA-Ames and NASA-Langley, NIA); universities (PSU, UMD, GIT); Germany (DLR, Univ. of Stuttgart); France (Onera); England (Univ. of Glasgow); Japan (JAXA); and South Korea (KARI, Konkuk University). A plethora of different computational investigations across the globe have used these data to both validate new simulation methods and to understand the physics of a rotor encountering blade vortex interactions (BVI).

These computational investigations have included the gamut of engineering assumptions included in comprehensive rotorcraft methods through computational fluid dynamics (CFD) coupled with computational structural dynamics (CSD) and computational aeroacoustics (CAA) methodologies. Individual or small collaborative efforts have been published and have resulted in advancements in the state of the art regarding modeling issues and numerical methods development. However, it has been difficult to assess the overall state of the art and best practices for all major (structured, unstructured, and hybrid) CFD/CSD approaches given the differences in the assumptions and presentation of the data in these works.

This effort gathers published and unpublished simulation results from the international team of experts shown in Table 1 who have been studying the HART II data set using CFD/CSD coupled methodologies. This compendium of results establishes simulation and modeling guidelines, provides a summary of state-of-the-art BVI CFD/CSD predictions, and explores the use of higher harmonic control (HHC) to reduce or eliminate BVI. This paper also provides direction for future experimental and simulation efforts, such as the international STAR collaboration. A companion paper (Ref. 2) explores the same parameter and model space, but analyzes the ability of lower-fidelity aerodynamics (finite-state, prescribed and free wake models) to capture the physics of the rotor.

## HART II EXPERIMENT

In 2001, the second Higher-Harmonic Control Aeroacoustic Rotor Test (HART II) was performed in the 8m ×

**Table 1. Partners and Codes**

Partner	Partner label	CFD Code	CSD Code
U.S. Army Aero-flightdynamics Dir.	AFDD-1	OVERFLOW	CAMRADII
U.S. Army Aero-flightdynamics Dir.	AFDD-2	NSU3D-SAMARC	RCAS
NASA-Langley	NL-1	OVERFLOW	CAMRADII
NASA-Langley	NL-2	FUN3D	CAMRADII
Georgia Institute of Technology	GIT-1	FUN3D	DYMORE4
Georgia Institute of Technology	GIT-2	GENCAS	DYMORE2
Konkuk University	KU	KFLOW	CAMRADII
University of Maryland	UM	URNS	UMARC
German Aerospace Center	DLR	N/A	S4

6m open-jet facility of the German-Dutch wind tunnel (DNW) in a cooperative American-French-German-Dutch effort (Ref. 3). The model rotor consisted of a Mach- and dynamically-scaled BO105 rotor blade. Data available for comparison include blade motion, sectional air loads, pressure distributions along the leading edge, tip vortex trajectories and flow fields, in addition to acoustic radiation. Important variables that define the simulation conditions for this experiment are summarized in Table 2.

A detailed description of the HART II data and how they were measured will not be given in this paper, as this is available in the test documentation and has been reported in numerous papers and reports (Refs. 1, 3–7). The reference rotor condition in this work is the HART II Baseline case (BL).

Due to wind tunnel interference, the rotor thrust deflects the slip stream, reducing the effective angle of attack to approximately  $\alpha = 4.5^\circ$ . This condition results in descending flight where strong blade-vortex interaction (BVI) occurs in the first quadrant ( $\psi \approx 50^\circ$ ) and the fourth quadrant ( $\psi \approx 300^\circ$ ) on the rotor disk where the vortex axis and the blade leading edge are approximately parallel to one another.

To evaluate the ability of higher harmonic control to reduce or eliminate the BVI, HHC with 3/rev and a blade root pitch control angle of  $\Theta_3 = 0.8^\circ$  was applied at a phase of  $\psi_3 = 300^\circ$  to reduce BVI noise radiation (minimum noise case, MN) and at  $\psi_3 = 180^\circ$  to reduce rotor vibrations (minimum vibration case, MV). Both of these HHC cases<sup>1</sup> illustrate the significant impact that HHC can have on BVI-related artifacts, such as noise and vibration.

This effort examines the following data from experiment across the CFD/CSD simulations: tip blade motion compared to experiment, sectional aerodynamic loading ( $C_n M^2$

and  $C_m M^2$ ) at the 87% radial station, flap and lag bending moments at the 17% radial station, torsion moment at the 33% radial station, lateral tip vortex positions at the  $\pm 70\%$  radial station in the hub coordinate system, and global trim data such as shaft angle, trim controls and targets. Given the length and complexity of this current effort, aeroacoustic simulation evaluations are not included.

## COMPUTATIONAL METHODOLOGIES

The computational methodologies applied in this effort consisted of computational fluid dynamics modules (CFD methods) coupled with computational structural dynamics modules (CSD) to provide aeroelastic simulations. As noted in Table 1, the methods applied were not exclusive to any one participant. Therefore, the methods are introduced by methodology name, rather than the participant name.

### Computational Fluid Dynamics (CFD) Methods

The partners applied six different CFD codes in this analysis, including four structured (OVERFLOW,URNS,GENCAS,KFLOW) and two unstructured (FUN3D,NSU3D) methods. The Helios framework combined a Cartesian background method (SAMARC) with the unstructured near-body solver (NSU3D). Two team members applied hybrid Navier-Stokes near-body solvers with free-wake farfield methods (GENCAS,URNS/PWAM). Each of these methods is briefly described, in particular the features which are pertinent to this effort.

**FUN3D** (Refs. 8, 9) solves the unsteady Navier-Stokes equations on unstructured grids, with several one- and two-equation turbulence models available to complete the system of equations. Inviscid fluxes are computed with second-order spatial accuracy by using one of several upwind schemes. Viscous fluxes are evaluated with a second-order discretization that is equivalent to a Galerkin scheme on tetrahedral meshes. FUN3D is a node-centered code; so

<sup>1</sup>The MN and MV naming convention was adopted from the 1994 HART I test. However, the HHC control angles from the HART I test are larger than the HHC control angles in the HART II test.

**Table 2. Summary of HART II Rotor Test**

Characteristic	Symbol	Value
Rotor geometry:		
Rotor radius	$R$	2 m
Blade chord	$c$	0.121 m
Number of blades	$N_b$	4
Rotor solidity	$\sigma$	0.077
Non-dim. root cutout	$r_a$	0.22
Non-dim. zero twist radius	$r_{tw}$	0.75
Blade linear twist	$\Theta_{tw}$	$-8^\circ/R$
Airfoil (trailing edge tab)		NACA23012
Wind tunnel data:		
Cross-section		8m $\times$ 6m
Air pressure	$p_\infty$	100.97 kPa
Air temperature	$T_\infty$	17.3° C
Air density	$\rho_\infty$	1.2055 kg/m <sup>3</sup>
Speed of sound	$a_\infty$	341.7 m/s
Wind speed	$V_\infty$	32.9 m/s
Mach number	$M_\infty$	0.0963
Hub center dist. to nozzle	$x_{hub}/R$	3.5
Hub pos. up of centerline	$z_{hub}/R$	0.4575
Operational data (BL case):		
Rotational speed	$\Omega$	109.12 rad/s
Hover blade tip Mach no.	$M_h$	0.639
Rotor shaft angle of attack	$\alpha_s$	5.3°
Wind tunnel interference angle	$\Delta\alpha_s$	-0.8°
Advance ratio	$\mu$	0.151
Rotor thrust	$T$	3300 N
Thrust coefficient	$C_T$	0.00457
Rotor loading coefficient	$C_T/\sigma$	0.0594
Roll moment	$M_x$	20 Nm
Pitch moment	$M_y$	-20 Nm
Rotor power	$P$	18.3 kW
Collective control at $r_{tw}$	$\Theta_{75}$	3.8°
Lateral cyclic control	$\Theta_C$	1.92°
Longitudinal cyclic control	$\Theta_S$	-1.34°
Mean steady el. tip twist	$\Theta_{el}$	-1.09°

the number of unknowns is directly related to the number of nodes in the grid. The code supports ‘mixed-element’ meshes in which the nodes may be connected into any combination of prisms, hexahedra, tetrahedra, and pyramids. Typical meshes use prisms near solid walls and tetrahedra outside of the boundary layer, with a limited number of pyramids providing transition between the two regions.

The solver has a robust implicit time-advancement scheme and a variety of mesh-motion options, including rigid, deforming, and overset meshes (Ref. 10). The time-advancement scheme makes use of an enhanced, second-order accurate backward difference scheme (Ref. 11) that is formally second-order accurate but has a leading-order

error term that is roughly one half that of the standard second-order scheme. In addition, a temporal-error controller (Ref. 12) is used to help insure that a sufficient number of subiterations are performed to drive the subiteration residual below the temporal error, thereby maintaining the design order of the scheme. For overset meshes, the DiRTlib (Ref. 13) and SUGGAR++ (Ref. 14) codes are used to facilitate communication between disparate zones in the mesh.

General mesh motion and robust time advancement are crucial for rotorcraft applications, where the flow is fundamentally unsteady, and the flexible rotor blades undergo large motions relative to the fuselage. O’Brien (Ref. 15) first applied the FUN3D solver to rotorcraft simulations, with the restriction of rigid blades in prescribed motion. Subsequent modifications (Ref. 16) resulted in a more general rotorcraft capability, with the ability to account for aeroelastic effects and trim via coupling with the Comprehensive Analytical Model of Rotorcraft Aerodynamics and Dynamics II (CAMRADII) code (Ref. 17). In separate efforts, Abras (Ref. 18) loosely coupled and Reveles et al. (Ref. 19) tightly coupled FUN3D with the DYMORE CSD code (Ref. 20).

Loose coupling (applied in this effort) between FUN3D and the CSD methods is implemented via the loosely coupled delta airloads strategy outlined in Ref. 21, and thus is appropriate to steady, level flight. The coupling is achieved via file exchange or Python scripting, and either approach is governed by a shell script that orchestrates the execution of the codes and provides restart, post-processing, and archiving functions. A typical coupled simulation proceeds as follows. First, a trimmed CSD solution is obtained with the CSD internal aerodynamics model, typically with a simple uniform or finite-state inflow. Blade displacements for one complete revolution are output by the CSD module for the first pass through FUN3D, where typically two complete revolutions are performed to remove large initial transients. FUN3D extracts airloads at selected stations along the rotor blades to obtain the airloads for one complete revolution.

Delta airloads from the previous coupling cycle are computed and passed to the CSD code, which then determines a new trim solution and blade motions. The process is then repeated until convergence, although for subsequent cycles FUN3D is run for only  $2/N_b$  revolutions between coupling cycles ( $1/N_b$  revolution is a minimum; the extra  $1/N_b$  revolution helps damp out transients during initial coupling cycles). This coupling strategy has not been examined for optimality; however, it has proven to be a robust strategy (stable and convergent). The coupling process is deemed to have converged when 1) trim control angles reported by the CSD code vary by less than  $0.01^\circ$  between coupling cycles, and 2) the thrust values obtained by integrating the sectional data provided by FUN3D and the corresponding data computed by the CSD code at the same sectional and azimuthal

locations, agree to within 0.1%. Fewer than 10 coupling cycles are usually required to meet these criteria.

**GENCAS** (Generic Numerical Compressible Airflow Solver) (Refs. 22, 23) is a generic Reynolds Averaged Navier-Stokes (RANS) solver including Hybrid Navier-Stokes/Free-wake method. In this hybrid method, only a single blade is modeled with the RANS solver. The effect of other blades is accounted for by a bound vortex and tip vortices. The free-wake model consists of a tip vortex from each blade shed from the tip periodically with the maximum bound vortex strength defined at the time at which it is shed. The effect of these tip vortices on the RANS solver is applied through outer surface boundary condition using Biot-Savart law.

GENCAS is coupled with the CSD solver, DYMORE version 2.0 (DYMORE2), and the delta airloads loosely coupled approach (Ref. 21) is applied to obtain the aeroelastic simulation. DYMORE runs with its own lifting line model as the first step, then the blade motion including pitch control and elastic deformation from DYMORE is fed into GENCAS. GENCAS interpolates the deformation data including three linear and three angular deformations using spline interpolation, as DYMORE2 is run at larger azimuthal time steps than the GENCAS solver. The delta airloads are then computed and provided to DYMORE.

**Helios** (Refs. 24, 25), under development by the U.S. Army through the CREATE program, is a multi-disciplinary computational platform. Helios includes software components responsible for near-body (NSU3D) and off-body (SAMARC), domain connectivity (PUNDIT), rotorcraft comprehensive analysis (RCAS or CAMRADII), mesh motion and deformation (MMM), a fluid-structure interface module (RFSI) and a fluid-flight dynamics interface (FFDI) module. All these components are interfaced together using a flexible and light-weight Python-based infrastructure called the Software Integration Framework (SIF). Figure 1 shows a schematic of the SIF. To preserve modularity, all data transfer between components occur through the SIF and no component is allowed to “talk” directly to another component. The parallel execution of the SIF is accomplished using pyMPI.

Helios employs an innovative dual-mesh paradigm that uses unstructured meshes in the near-body for ease of mesh generation and Cartesian meshes in the off-body for better accuracy and efficiency. The two mesh types overlap each other with data exchange between the two systems managed by a domain connectivity formulation. The unstructured meshes are body-conforming and are comprised of a mix of tetrahedrons, prisms and pyramids. The Cartesian meshes are managed by a block-structured mesh system, which has the ability to conform to the geometry and solution features.

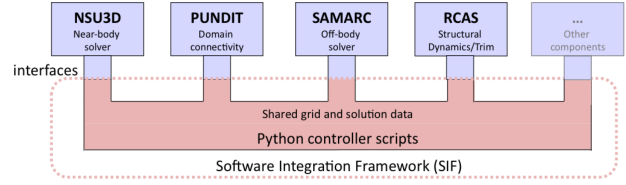


**Fig. 1. Python-based infrastructure in Helios**

The near-body solver NSU3D uses a node-centered finite-volume scheme that is spatially second-order accurate. An edge-based data structure is used, which facilitates flux computations on the edges of the median-dual control volume. Time-accurate computations employ a second-order accurate backwards Euler algorithm with subiterations applied in dual-time algorithm to converge the non-linear problem at each time-step. The implicit solution algorithm applies multigrid with line-Jacobi relaxation to smooth each grid level. The single-equation Spalart-Allmaras model is used to model turbulence.

The structured adaptive Cartesian code SAMARC is used for the off-body Cartesian grid. SAMARC solves the Euler equations using a fifth-order spatial discretization and third-order Runge-Kutta time integration. The off-body grid has the ability to automatically adapt to the unsteady geometry and solution features.

Both NSU3D and SAMARC run in parallel. PUNDIT manages overset domain connectivity on the partitioned grid system. It automatically determines which grid and solver apply in different regions of the flow field, computes the interpolation operations between different grid systems, and manages the parallel exchange of data.

Rotorcraft structural dynamics and trim are solved using a CSD method, currently either Rotorcraft Comprehensive Analysis System (RCAS) (Ref. 26) or CAMRADII (Ref. 17). At each coupling iteration the aerodynamic forces on the blade computed by CFD are passed to the CSD code. The CSD code computes the deflections based on the CFD forces and passes the deflections back to CFD at some  $n/N_b$  intervals, where  $n$  is an integer (typically one or two) and  $N_b$  is the number of rotor blades. This sequence is repeated until the loads and deflections converge to a periodic steady-state solution using the delta-airloads approach (Ref. 21).

**KFLOW** is a structured RANS solver capable of solving time-accurate moving body problems by employing a Chimera overlapped grid system (Refs. 27, 28). A second-order accurate, dual-time stepping scheme, combined with a diagonalized alternating-directional implicit (DADI) method, is used for the temporal scheme. For the spatial discretization, a fifth-order weighted essentially



non-oscillatory (WENO) scheme is used for the inviscid fluxes, and the central difference scheme is adopted for the viscous fluxes.

The delta-airloads loose coupling approach (Ref. 21) has been adopted to systematically couple the CAMRADII and KFLOW codes. Both the control trim angles and blade motion data are computed from the CSD code, while KFLOW generates the CFD airloads acting on the blades. The delta airloads between the two codes is calculated and fed into the CSD code to obtain updated blade motions and trim angles. This process is repeated until the airloads and trim values are generally within a tolerance of 0.1% between coupling iterations. Since the blade motion data from the CSD module are obtained at significantly larger time steps than the corresponding CFD module, a fitting technique based on the mode shapes and a Fourier series (Ref. 29) is employed to obtain sufficiently smooth curves to be interpolated and applied in the CFD analysis.

**OVERFLOW2** (Ref. 30) is a structured mesh methodology developed by NASA and has been extensively applied to rotorcraft configurations, including CFD/CSD loose coupling (for example, Ref. 18, 21, 31). Spatial discretization formulations that span second- to sixth-order accuracy are available to resolve the inviscid terms and in conjunction with several dissipation schemes. Turbulence simulation options include a large selection of RANS, hybrid RANS-LES, and LES/VLES turbulence methods. In this effort, the Spalart-Allmaras (SA) and Spalart-Allmaras Detached Eddy Simulation (SA-DES) models were applied by AFDD-1 and NL-1 partners, respectively. The versions of OVERFLOW applied in this effort are 2.2c (NL-1) and 2.1ac (AFDD-1).

The aeroelastic behavior of rotors can be modeled using a loosely- or tightly-coupled CFD/CSD strategy (Refs. 19, 21, 32). The loosely coupled CFD/CSD approach (used in this effort) applies the delta airloads technique (Ref. 21), which exchanges data between the CFD and CSD codes at regular intervals defined as integer multiples of the blade-rotor fraction of  $n/N_b$ . OVERFLOW has been coupled with the CAMRADII (Ref. 17), RCAS (Ref. 26), and DYMORE (Ref. 20) CSD codes.

**URNS/PWAM** (Transonic Unsteady Rotor Navier-Stokes) is a computational fluid dynamics solver capable of solving unsteady aerodynamics flows. It applies a second-order backward difference method using Lower-Upper Symmetric Gauss Seidel (LUSGS) (Refs. 33, 34) for time integration. Six Newton subiterations are used to remove factorization errors and recover time accuracy for unsteady computations (Ref. 35). The inviscid fluxes are computed with Roe's flux differencing and MUSCL reconstruction. The viscous fluxes are computed with second-

order central differencing. The Baldwin-Lomax turbulence model is used for RANS closure. The effects of the far field wake are prescribed by the field-velocity approach.

The free-wake module, PWAM (Parallel Wake Analysis Module) developed at the University of Maryland (UMD) is a time accurate, efficient, scalable parallel implementation of the vorticity transport equations in a Lagrangian domain (Ref. 36). The wake geometry is discretized into vortex filaments whose strengths are calculated from the provided aerodynamic forcing. The convection velocity of each vortex filament is computed by aggregating their mutual influences and the freestream convection velocity. The mutual influence between the vortex filaments can be computed using the Biot-Savart law. The resulting equations for wake positions are integrated in time using a second-order Runge-Kutta scheme. A 2.5 degrees discretization is used in both azimuthal and wake age directions. Spectral interpolation in azimuth and cubic spline interpolation in the radial direction are chosen to suit the CFD time discretization. The trailed vortex system consists of a root vortex and a tip vortex which convect for two revolutions. To account for the possibility of negative lift across the rotor disk and generation of two counter rotating vortices, the tip vortex release point is allowed to move to the first radial point of negative lift in the outer portion of the blade. The radial direction was discretized using 60 elements. The near wake region spanned over 30 degrees before rolling up into a tip vortex, whose strength is the maximum blade bound circulation found in the outer half of the blade. Vortex aging follows Squire's law (Ref. 37) and the swirl velocity model is due to Scully's formulation, see Ref. 38.

The coupling between the various solvers is implemented using Python scripts. For each solver, a Python class interface is created, which interacts with the FORTRAN modules using the Fortran to Python Interface generator (F2PY). Parallelization of the code is achieved using pyMPI. The Python NumPy library is used for array manipulation and data exchange between the solvers. A loose coupling methodology is employed where blade deflections, wake geometry, and airloads are exchanged between the solvers at every revolution. Data from the different codes are interpolated using spectral interpolation in azimuth and cubic spline interpolation in the radial direction.

Rotor trim is performed to target thrust and moments by coupling to the comprehensive code UMARC (University of Maryland Advanced Rotorcraft Code). UMARC provides structural dynamics modeling and rotor trim via the delta-airloads loose coupling technique (Ref. 21). A free-flight propulsive trim algorithm is used. Once a converged aerodynamic solution is obtained, the new airloads are sent to the structural dynamics solver. The steady integrated loads are computed at the hub and compared to the prescribed thrust and moments, leading to updated values of

the control angles and deflections, see Ref. 39.

### Computational Structural Dynamics Methods

The CFD/CSD coupling approaches apply four different CSD methods: CAMRADII, DYMORE, RCAS, and UMARC. In addition, the CFD/CSD results are compared and contrasted to a comprehensive method, S4, that has been shown to be consistent with numerous other comprehensive methods (Ref. 2). Additional details of these CSD methods can also be found in Ref. 2.

**CAMRADII** (Comprehensive Analytical Model of Rotorcraft Aerodynamics and Dynamics II) (Ref. 17) models the rotor beam with finite nonlinear beam elements. Each nonlinear beam element has fifteen degrees of freedom (four flap, four lead-lag, three torsion, and four axial). The fully-coupled, nonlinear equations of motion are solved for the wind tunnel trim condition. Rotor blade motion is computed using the harmonic balance method. The trim solution is obtained with a Newton-Raphson method with the Jacobian matrix numerically computed. The trim targets are thrust, roll and pitching moment.

**DYMORE** (Ref. 20) is a nonlinear flexible multi-body dynamics analysis code developed at Georgia Institute of Technology (GIT). It has various multi-body libraries such as rigid bodies, mechanical joints, elastic springs, dampers, nonlinear elastic bodies such as beams, plates, and shells. Although DYMORE has not been developed specifically for rotorcraft applications, its powerful multi-body modeling capability based on an arbitrary topology allows it to be widely used in the rotorcraft analysis. DYMORE uses the finite-element method (FEM) in time domain without relying on a modal reduction technique.

Two different versions of DYMORE (2 and 4) were applied in this study. While there are various differences in the two methods, the primary difference that pertains to this work is in the trim algorithm. In DYMORE2, an auto pilot method (Ref. 40) is used for the trim analysis, while in DYMORE4 a quasi-steady trimmer (Refs. 19,41) that is designed to improve the efficiency of the trimming process is applied for either loose (used here) and tight coupling.

**RCAS** or the Rotorcraft Comprehensive Analysis System (Ref. 26) models the rotor CSD and trim in CFD/CSD coupling. RCAS is the comprehensive code developed and maintained by the U.S. Army Aeroflightdynamics Directorate (AFDD) in partnership with Advanced Rotorcraft Technology, Inc. RCAS is a state-of-the-art, finite-element based, multibody dynamics code with capabilities for modeling large deformations, composite nonlinear beam, full

aircraft trim and maneuvers. The non-linear equations of motion are constructed with a finite-element beam element formulation, and the trim is found with the Newton-Raphson method.

**S4** is DLR's high resolution fourth-generation rotor simulation code (S4). S4 can be used for any kind of active rotor control with respect to performance, dynamics, and noise (Ref. 42) and to support wind tunnel testing. A finite element method (Ref. 43) based on the Houbold-Brooks formulation (Ref. 44) performs the modal analysis, i.e., it computes the coupled mode shapes and natural frequencies in vacuo. The beam elements used have 10 degrees of freedom (deflection and gradient at both ends for flap and lag; twist angle at both ends for torsion). The major component of the mode shapes is then represented analytically as a seventh-order polynomial in the radial coordinate direction. All mass integrals required in the differential equations of motion, as well as for computation of the blade root forces and moments, are evaluated in post processing. This includes mechanical coupling like flap-torsion coupling caused by an offset of the mass axis from the elastic axis. Thus, the structural discretization used for modal analysis is completely independent of the aerodynamic discretization used in rotor simulation.

In a second step and independent from the FEM, the rotor simulation itself solves the dynamic response problem of these modes (which are reduced to their major component) subjected to the aerodynamic loading in form of a modal synthesis. In the computations shown in this paper, four flap modes, two lag modes and two torsion modes have been retained, which covers the frequency range up to 10/rev. A higher number of modes have also been examined, but the mode deflections were found to be so small that they do not contribute to the results and thus were omitted.

Trim to the prescribed thrust and hub moments is performed by using fourth-order Runge-Kutta time integration with azimuthal increments of  $1^\circ$  (intermediate step at every  $0.5^\circ$ ). The radial discretization of the airfoil portion of the blade features forty elements, non-equidistantly distributed with higher density at the blade tip so that every blade element covers the same ring surface of the rotor disk. The trim algorithm iteratively computes the derivatives of thrust and moments with respect to the control angles and based on these, the corrective angles for the next trim step are evaluated.

The unsteady section aerodynamic forces and moments are computed based on a semi-empirical math model (Ref. 45). The model accounts for airfoil motion and separately for vortex-induced velocity fluctuations with different deficiency functions. Fuselage-induced velocities at the rotor blades are also included (Ref. 46).

The prescribed wake geometry (Ref. 47) is updated once a trim cycle with updated blade motion and airloads. The influence coefficients of the new wake geometry are updated before the next trim cycle starts. During the trim, the induced velocities of the far wake are updated every few revolutions to account for the variations of changing airloads and changing vortex strengths as a consequence of these. Wake perturbations due to harmonic air load distribution within the rotor disk are accounted for as well (Ref. 48).

**UMARC**, the University of Maryland Advanced Rotorcraft Code provides structural dynamics modeling and rotor trim. The comprehensive aeroelastic analysis is based on a finite-element methodology (Ref. 49). The four blades are modeled as second-order, non-linear isotropic Euler-Bernoulli beams. They are divided into twenty radial elements undergoing coupled flap, lag, torsion, and axial degrees of freedom based on Refs. 50 and 51. Modal reduction is limited to the first ten dominant natural modes (five flap, three lag, two torsion). The structural dynamics equations are integrated in time by using the finite-element-in-time procedure that uses twelve equal temporal elements with six points within each element. This results in an effective azimuthal discretization of  $5^\circ$ . To compute the local bending moments, the force summation method is used.

## COMPUTATIONAL GRID AND SIMULATION DETAILS

Prior to discussing the simulation results, short descriptions of the CFD grids, CSD structural models, CFD/CSD run options, and timing are included in this section. Table 3 provides a quick reference for the different grids, while Table 4 presents the run options selected by each partner. In this section, each partner's inputs are included; the reader is referred to Table 1 for partner labels.

To assess the computational requirements of these computations, Table 5 is included. However, these values should be approached with some caution as the intentions of the partners in the study are different. Several partners have deliberately applied large, refined grids in an attempt to resolve specific physics, while others have attempted to compute results based on engineering-level grids and methods. Thus, to make direct conclusions of the computer resources would be naïve and could be misleading. Thus the approach of this analysis is to understand the needs and physics associated with each approach, but not to advocate one code or methodology over another. In addition, it should be noted that the computational times reported in Table 5 have not been adjusted for processor speeds or interconnectivity approaches.

**AFDD-1:** Figure 2(a) shows the OVERFLOW fuselage surface grids with a cut through the off-body volume grids.

The blade grid system consists of blade grid, root cap and tip cap, and the dimensions of these grids are  $295 \times 89 \times 53$ ,  $169 \times 49 \times 53$ , and  $181 \times 81 \times 55$ , respectively. The rotor near-body grids have a total of 10.8 million grid points. The fuselage grids consist of nine grids/patches including cap grids in the fuselage nose, the end of the sting and the top of the hub cylinder. The near-body grids were formed by extending the surface grids to approximately one chord length in the normal direction, and the wall function,  $y^+$  was estimated a priori as unity for the first mesh from the surface. The fuselage near-body grids have about 0.7 million grid points. The off-body grids have a level-1 mesh spacing of 0.10 chords near the rotor and fuselage surfaces. The complete grids of the rotor and fuselage have 35.5 million grid points. Further detailed discussion is available in Ref. 52.

A sixth-order central difference scheme resolved the configuration using a Spalart-Allmaras turbulence model for closure. The thin-layer Navier-Stokes option was applied at the surface, and the off-body grids were resolved with the Euler equations. A first-order time stepping scheme with  $1/20^\circ$  time step and one subiteration was applied for temporal integration.

The simulations were run on Pleiades at NAS on 64 3GHz Intel Xeon (Harperton) processors. Total wall clock time (on 64 processors) for a coupled CFD/CSD solution for 4 rotor revolutions was 84 hours.

**AFDD-2:** Figure 2(b) shows the computational grid consisting of a near-body mesh that contains a fuselage with 3.6M nodes. While the fuselage remains fixed, the rotor meshes move and deform during the simulation. Two near-body unstructured grids are used for the rotor blades to understand the effect of the grid on the airload predictions. The near-body grids extend to about one chord length from the surface of the rotor blade. The coarse near-body mesh has 3.7M nodes which includes clustering at the blade tip trailing edge. The fine blade mesh has 12.5M nodes.

The off-body domain extends approximately 80 chord lengths in each direction. Six and seven levels of off-body grid are used with the coarse and fine near-body meshes respectively. The finest level spacing in the off-body mesh is 10%-chord with six levels and 5%-chord with seven levels.

A  $0.1^\circ$  time step is used for time marching with 25 subiterations per time step for the near-body and 2 sub-steps per time step for the off-body (determined automatically based on CFD conditions of the finest level grid). The CAM-RADII calculations used a  $5^\circ$  time step. Four revolutions were needed to get a fully converged solution. Fine near-body mesh with 5% chord spacing in off-body is used for the baseline case. Minimum noise (MN) and minimum vibration (MV) cases use a coarse near-body mesh with 10% chord spacing in the off-body.



**Table 3. Computational Grid Characteristics**

Partner Label <sup>a</sup>	Grid Type	Fuselage Grid Nodes	Single Blade Grid(s) Nodes	Normal Spacing ( <i>c</i> )	Fuselage Modeled?
AFDD-1	Structured	0.7M	2.7M	$1 \times 10^{-5}$	Yes
AFDD-2	Unstructured <sup>b</sup>	3.6M	3.0M	$1 \times 10^{-5}$	Yes
GIT-1	Unstructured	9.2M	1.2M	$1 \times 10^{-5}$	Yes
GIT-2	Structured <sup>c</sup>	N/A	1.6M	$5 \times 10^{-5}$	No
NL-1	Structured	13.9M	6.0M	$8 \times 10^{-5}$	Yes
NL-2a	Unstructured	9.2M	1.2M	$1 \times 10^{-5}$	Yes
NL-2b	Unstructured	17.6M	1.6M	$1 \times 10^{-5}$	Yes
KU	Structured	2.5M	1.5M	$1 \times 10^{-5}$	Yes
UMD	Structured <sup>c</sup>	N/A	1.1M	$1 \times 10^{-5}$	No

<sup>a</sup> See Table 1.

<sup>b</sup> Unstructured near-body grid with a Cartesian background grid.

<sup>c</sup> Hybrid method with a structured near-body grid with a wake model.

**Table 4. Computational Run Options**

Partner Label <sup>a</sup>	Spatial Order	Temporal Order	CFD Time Step	Subiterations	Turbulence Model	CSD Time	Spring Stiffness (Nm/rad)
AFDD-1	5	1	0.05°	1	Spalart-Allmaras	15°	1,200
AFDD-2	2	2	0.10°	25	Spalart-Allmaras	5°	1,200
GIT-1	2	2	1.00°	4,30 <sup>b,d</sup>	Spalart-Allmaras	5°	1,632
GIT-2	3	1	0.10°	4	SA-DES	1°	1,000
KU	5	2	0.20°	10	<i>k-<math>\omega</math></i> Wilcox-Durbin	15°	1,000
NL-1	5	2	0.25°	20 <sup>c</sup>	SA-DES	15°	1,200
NL-2	2	2	1.00°	30 <sup>b</sup>	Spalart-Allmaras	15°	1,200
UMD	3	2	0.25°	6	Baldwin-Lomax	5°	2,336
DLR	0	2	1 <sup>°e</sup>	4	none	1°	400

<sup>a</sup> See Table 1.

<sup>b</sup> With a temporal-error controller

<sup>c</sup> Or two orders of residual reduction, whichever occurs first

<sup>d</sup> Initial coupling iterations applied 4 subiterations to acceleration solutions, then switched to 30

<sup>e</sup> Wake model time step

**Table 5. Computational Costs**

Partner Label <sup>a</sup>	Processor Speed (GHz)	Number of Cores	Number of Revolutions	Total CPU Time <sup>b</sup> (Hrs)
AFDD-1	3	64	4	5,500
AFDD-2 <sup>c</sup>	2.88	256	4	8,700
AFDD-2 <sup>d</sup>	2.88	512	4	76,900
GIT-1	2.8	128	6–7	21,900–25,500
GIT-2	2.67	6 (initial) + 9 (full)	4(initial) + 4(full)	700
NL-1	3.0	512	5	76,800
NL-2a	3.0	241	7–8	40,300–50,400
NL-2b	3.0	257	7–8	73,300–88,400
KU	2.93	96	10.5	22,200
UMD	3.2	16	6–7	2,900–3,400
DLR	2.0	1	250	0.07

<sup>a</sup> See Table 1.

<sup>b</sup> Number of processors or cores times number of revolutions, rounded to the nearest 100 Hrs, except for DLR and GIT-2.

<sup>c</sup> A less refined grid was applied to the MN and MV cases.

<sup>d</sup> A refined grid was applied only to the BL case.

The blade was modeled by a series of finite beam elements with each element having three translational (axial, lead-lag, and flap) and three corresponding rotational degrees-of-freedom (DOF), which results in fifteen DOFs for each beam element. The blade frequencies were calculated with 5° collective in vacuo, and ten finite beam elements were used to model each blade in both cases. The trim condition satisfies the wind tunnel trim targets (thrust, roll moment, and pitching moment) using the trim variables of pitch collective, lateral cyclic, and longitudinal cyclic control.

The total central processing unit (CPU) time for the coarse mesh, which was used for the MN and MV cases, is 42.3 hours using 256 Nehalem-EP 2.8 GHz processors with infiniband connections on the Dell PowerEdge Linux quad-core cluster located at Maui High Performance Computing Center. Fine mesh computations used for the baseline case required 150 hours using 512 processors. These simulation times were based on four rotor revolutions.

Additional details and descriptions related to these simulations can be found in Refs. 53 and 54.

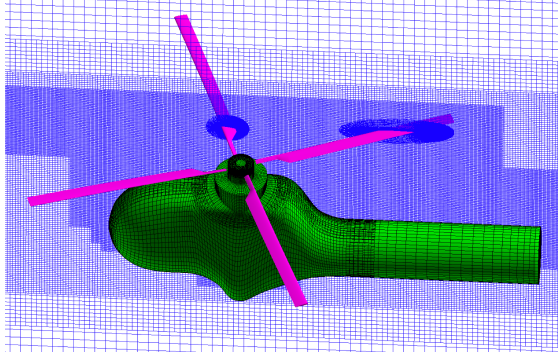
**GIT-1:** The same 14M grid and run conditions used by NASA (NL-2a) were applied at Georgia Tech so that the differences in the two structural models (CAMRADII and DYMORE4) could be assessed. The grids and run conditions are described in the **NL-2** section.

As the HART II rotor lacks flap and lead-lag hinges between the hub and the blades, the model attaches the blades directly to the hub, while the inboard portion of the blade, comprised of a stiff elliptical cross-section is permitted to

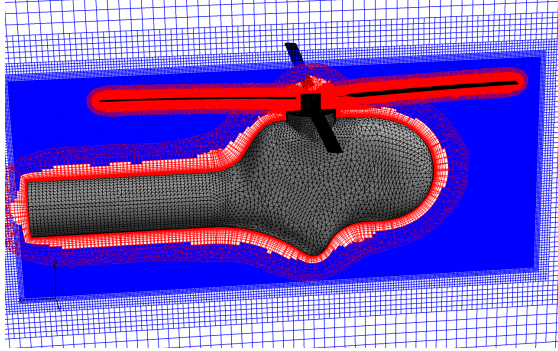
bend elastically to absorb some of the bending moment that would otherwise be transferred to the hub. The DYMORE4 model has a number of simplifications compared to the experimental rotor. Most of the hub hardware is not modeled and the blades are attached to a revolute joint with a pitch spring to represent the pitch link at the hub axis. The pitch spring stiffness of 1,632 Nm/rad was obtained by “tuning” the torsional response to the first torsion mode at 100% RPM. Each rotor blade is modeled as two beams to separate the inboard “flex beam” and the rotor blade. The flex beam is constructed from a single third-order finite element. The main blade consists of eight third-order elements, which predict the first torsion frequency at 100% RPM to within 0.5% of the nominal value.

The simulations were made using 128 AMD 2.8GHz Opteron 64-bit processors on the NAVO SUSE Linux cluster. The simulations were trimmed within 4.5 revolutions (BL, 70.4 wall clock hours), 6.5 revolutions (MN, 109.2 wall clock hours), and 8 revolutions (MV, 135 wall clock hours).

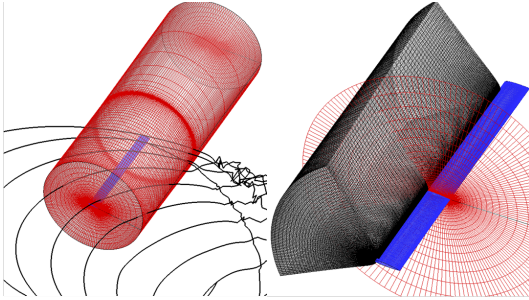
**GIT-2:** There are two sets of grids that are needed to model the single rotor blade, shown in Fig. 2(c). The main blade O-grid includes  $171 \times 78 \times 69$  grid points in the chord, radial, and normal directions, respectively. Once the coupling process is finished and converged blade motion is obtained, an embedded grid technique is applied for several additional revolutions to obtain a refined final solution. An embedded grid was placed forward of the blade extending the entire radial distance of CFD grid to more accurately capture incoming vortices. The total number of grid points



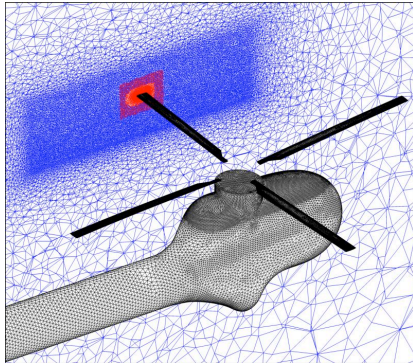
(a) OVERFLOW structured overset grid



(b) Helios unstructured near-body and Cartesian off-body grid



(c) GENCAS hybrid grid system



(d) FUN3D 14M node overset unstructured grid

**Fig. 2. Sampling of CFD grids applied in the HART II analyses**

including the embedded grid is 1.6 million, and the first cell off the wall is approximately  $5 \times 10^{-5}c$ . The average  $y^+$  value is about 5.9 and includes 8–9 cells located inside the estimated boundary layer at 70% radial location.

The blade was rotated  $0.1^\circ$  per time step. Roe's finite-difference scheme was used with third-order spatial accuracy, and second-order central differencing was used for viscous fluxes. A first-order implicit LU-SGS algorithm integrated the simulation temporally with optional subiterations. Four subiterations were used in final solution process with the embedded grid. However, subiterations are not used during the initial coupling process. The SA-DES model with a rotational correction was applied for turbulence closure. A total of five revolutions of free-wake filaments were included in the wake computation, and the wake was convected at every  $1^\circ$  with local flow velocity.

The rotor was mounted at a shaft tilt angle of  $4.5^\circ$  backward without a fuselage model. The DYMORE2 model consisted of a revolte joint at the hub center, root-retention from hub to pitch bearing location (0.075m), followed by the BO105 sectional rotor blade. The root-retention and the blade were modeled as beams. The pitch link was not modeled, and the pitch spring stiffness was set to 1,000 Nm/rad. A time step of  $15^\circ$  was used, and the GENCAS CFD solver was run until periodic solution is obtained.

Simulations were run on a workstation with 12 Intel Xeon processors with 2.67 GHz clock speed. Each case used six processors. Per each coupling iteration cycle, a maximum of four revolutions required nine CPU hours without the embedded grid and subiterations. For the final coupling iterations, nine processors were used, and the total CPU time for four revolutions (14,400 time steps) with the embedded grid and adding four subiterations was 35 hours.

**NL-1:** The simulations were run with dual time stepping for a physical time step of  $0.25^\circ$  and a maximum of 20 Newton subiterations per time step. Fewer subiterations were applied if a two order of magnitude drop in residual is achieved before 20 subiterations. A sixth-order central difference scheme resolved the inviscid terms. The Spalart-Allmaras Detached Eddy Simulation (SA-DES) turbulence model with a rotational/curvature correction (SARC) was applied for RANS closure.

The airfoil part of each rotor blade is an O-mesh with  $192 \times 273 \times 65$  nodes in the streamwise, radial, and normal directions, respectively. Each blade also includes tip and root grids, which are both  $181 \times 109 \times 65$ . The first grid cells normal to the surface are located at  $8.26 \times 10^{-5}c$ . The grids extend to 1.5 chord lengths normal to the blade surface. The off-body level 1 grid covers the entire rotor and fuselage with a grid spacing of  $0.0825c$ . The farfield grid extends to 50 meters (25R in all directions). Before grid

splitting, the number of grid points in the total grid is 158M nodes.

The structural model is based on finite nonlinear beam elements. Each nonlinear beam element has nine degrees of freedom (two flap, two lead-lag, two torsion, and three axial). Each blade is modeled using ten nonlinear beam elements with one rigid element inboard of the pitch bearing. The fully-coupled, nonlinear equations of motion are solved for the wind tunnel trim condition. The trim procedure is accomplished at an azimuthal resolution of  $15^\circ$ . The torsional spring value was determined to be 1,200 Nm/rad.

The simulations were run on Pleiades at NAS on 512 Intel Xeon (Harperton) processors. Total wall clock time (on 512 processors) for a coupled CFD/CSD solution for five rotor revolutions (7,200 time steps) was 140 hours.

Additional details on this configuration, grids, and set of simulations, including aeroacoustic analysis, can be found in Refs. 55 and 56.

**NL-2:** The component unstructured grids for the over-set computations were generated with the VGRID v4.0 advancing-layer and advancing-front grid generation software package (Ref. 57). Grids generated with VGRID are fully tetrahedral. However, VGRID uses an advancing-layer technique to generate the boundary-layer portion of the grid, which allows prisms to be reconstructed in the boundary layer for use with FUN3D's mixed-element discretization. Mixed-element grids are used for all the FUN3D/CAMRADII results presented here. The four rotor blades and fuselage/drive system fairing are modeled, but the hub, linkages and wind tunnel walls are not. The component grids for the blades and fairing are assembled into a composite grid with the SUGGAR++ software. In the fairing grid, points are clustered in a 'tuna can' region surrounding the rotor disk, to allow better resolution of the vortex system. Results for two grids are presented, containing approximately 14 and 23 million nodes, respectively. In the smaller grid, the fairing component mesh contains approximately 9 million nodes, while in the finer mesh, the fairing component mesh contributes approximately 16 million nodes—the difference due to the number of nodes in the 'tuna can'. Grid spacing in the 'tuna can' is approximately 10% of the blade chord in the 14 million node mesh and approximately 7.5% blade chord in the 23 million node mesh. In both grid systems, each rotor blade is defined with approximately 20,000 surface nodes. Both grid systems have the same grid spacing near the blade surface, approximately 0.001% blade chord. Each blade grid contains 30 prism layers near the wall, these layers extend approximately 1.26% blade chord normal to the surface. The principle difference between the blade grids in the two systems occurs away from the blade surface, where grid-point spacing near the outer boundary is specified to be comparable to the 'tuna

can' spacing in the corresponding fairing grid. As a result, each blade grid in the 14 million node mesh contains approximately 1.2 million nodes while each blade grid in the 23 million node mesh contains approximately 1.6 million nodes. The blade grids are oriented so that the geometric pitch is zero at 0.75R in the reference (zero control angle) position. Figure 2(d) illustrates the surface meshes and a cut through the volume grid for the 14 million node mesh. In the cut through the mesh, blue corresponds to the fairing grid and red to the blade grid; the clustered region of the 'tuna can' is apparent in the fairing mesh.

For all the FUN3D/CAMRADII simulations presented here apart from the two different mesh sizes discussed above, the following run options were used. Inviscid fluxes were computed by using Roe's scheme (Ref. 58) with no flux limiters. The effects of turbulence were included via the Spalart-Allmaras model (Ref. 59). The enhanced, second-order backwards difference time-advancement scheme and temporal-error controller described previously were used with a time step corresponding to  $1^\circ$  azimuth change per step. The subiteration residual was targeted to be one order of magnitude lower than the temporal-error estimate for each time step; in case that criterion was not met, a maximum of 30 subiterations were permitted in any given step. The pitch bearing spring stiffness in the CAMRADII model was 1,200 Nm/rad.

Most of the results presented here were run on a cluster of 3.0 GHz P4 dual-core processors with 4 GB of memory per processor connected by Gigabit Ethernet. The FUN3D solver was run using 128 of these processors (256 cores). A large-memory P4 node with 64 GB of memory is available and one core of this node was used to run the SUGGAR++ code for overset connectivity, bringing the total number of cores used to 257. With these resources, the computational time per time step for the 23 million node mesh was approximately 345 seconds, and the time to complete one-half revolution of the rotor (the frequency at which CFD and CSD codes exchanged data) was approximately 17.5 hours.

For all three conditions (BL, MN, MV), convergence to rather tight tolerances for the control angles and CFD/CSD thrust deltas ( $0.1^\circ$  and 0.1%, respectively) required approximately 10 rotor revolutions.

**KU:** A moving overlapped Chimera grid system with two different systems of grids is employed: near-body structured grid and off-body Cartesian grid. The near-body grids extend  $1.5c$  in the normal direction from the blade surface. They are clustered near the leading edge, trailing edge, and blade tip regions. The cell spacing for the first grid point from the wall boundary is  $1.0 \times 10^{-5}c$  so that  $y^+$  remains below 3.0. The off-body grids consist of an inner region that extends four chord lengths above, three chord lengths below from the blade, and 1.5 chord lengths away from the



blade tip. The far field boundary is five times the blade radius,  $R$ . The off-body grids have a uniform spacing of  $0.1c$ . Overall, the rotor-fuselage model used has about 37.6 million cells: the near-body grid system has a dimension of  $321 \times 97 \times 49$  (chordwise, radial, and normal), while the off-body grid system has a dimension of  $161 \times 441 \times 401$  (vertical, lateral, and longitudinal).

The blade is discretized into finite-element beam segments having axial, lag bending, flap bending, and torsion degrees of freedom. A total of 16 beam elements are used to model the blade. In addition, a total of twelve dynamic modes are used to describe the blade dynamics of the HART II rotor. The nominal 1,000 Nm/rad pitch spring stiffness was applied for the computations. The reader is cautioned that this is not the same structural model labeled ‘KU’ described and presented in Ref. 2.

The time step size used is 0.2 degree azimuth (1,800 steps per revolution) for the present computation. The number of subiterations performed at each physical time step is ten to ensure the convergence of the CFD solution. The  $k-\omega$  Wilcox-Durbin scheme (Ref. 60) is employed for the turbulence model.

The computational resource used was an IBM PC-based parallel machine equipped with Intel i7-870 processor (2.93 GHz clock speed) having 116 cores and 2GB RAM per core. The CPU time consumed for a full revolution of the rotor was about 22 hrs when 96 CPUs were employed. About six coupling iterations, corresponding to 10.5 revolutions, were typically required to reach a trim condition.

**UMD:** The solver applies to each of the four rotor blades identical body-fitted C-O meshes consisting of 129 points around the wake and blade surfaces (of which 97 points are on the blade surface), 129 points in the radial direction, and 65 points in the normal direction. The grid spacing near the blade surface in the normal direction is approximately  $1 \times 10^{-5}c$ , and the value of  $y^+$  is kept to 1.0 with 20–30 normal cell points within the boundary layer at 70% $R$ .

The four blades are modeled as second-order non-linear isotropic Euler-Bernoulli beams. They are divided into twenty radial elements undergoing coupled flap, lag, torsion, and axial degrees of freedom. Modal reduction is limited to the first ten dominant natural modes (five flap, three lag, two torsion). The structural dynamic equations are integrated in time by using the finite-element-in-time procedure which uses twelve equal temporal elements, with six points within each element. This results in an effective azimuthal discretization of  $5^\circ$ .

A  $0.25^\circ$  azimuthal time step is used with the second-order backward difference method for time integration. Six Newton subiterations are used to remove factorization errors and recover time accuracy for unsteady computations.

The inviscid fluxes are computed using a third-order upwind scheme that uses Roe’s flux differencing with a Monotonic Upwind Scheme for Conservation Laws (MUSCL) reconstruction. The viscous fluxes are computed using second-order central differencing. The Baldwin-Lomax turbulence model is used for RANS closure.

These cases ran on 16 3.20 GHz Intel Xeon cores with 2GB of memory per core. Six to seven coupling cycles were required to obtain a converged solution, and each cycle required 30 wall clock hours.

**DLR:** The DLR S4 solver is described in the CSD methods section, and includes many of the details applied for the simulations appearing in this paper. An expanded discussion of the code can be found in Ref. 2.

The S4 code was run on a single core with a 2.0GHz processor of a Linux-based personal computer. The S4 algorithm is time marching, so 250 revolutions are needed to achieve convergence, including all trim cycles and wake updates. The fuselage is modeled in the S4 analysis. The total CPU time is 250 seconds or 0.0694 hours, excluding noise computations, which require an additional 40 seconds.

## STRUCTURAL DYNAMICS ANALYSIS

The team partners applied a number of different computational structural methods, as noted in Table 1. To evaluate the computational aerodynamics portion of these simulations, care was taken so that each method modeled the structural characteristics of the rotor as closely as possible to a single common configuration, as defined in the test documentation (Refs. 4, 5). To verify the structural model, the structural dynamic behavior of the rotor blade under in vacuo conditions was examined at  $0^\circ$  collective (referenced to the 75% radial station). This analysis was made by using the first ten mode shapes and natural frequencies. As there were no experimentally measured data at the nominal 100% RPM for these variables, comparison among the partners was evaluated. Experimental data were obtained for a fixed (non-rotating) frame (Ref. 61), and these are compared with the computational predictions. Some of these data are also compared in a companion paper (Ref. 2), which includes comprehensive model predictions. The different values plotted for measured first torsion nonrotating frequencies are extracted from the HART II test documentation (Ref. 4). The lower two values are the frequencies obtained from the instrumented blades (blades 1 and 4) while the two higher frequencies are extracted from the uninstrumented blades (blades 2 and 3).

While structural analysis provides a quantitative measure of the similarity of the different structural models used in this analysis, not all of the partners applied a modal analysis in their simulations. Specifically, the partners apply-

ing RCAS (AFDD-2) and DYMORE (GIT-1, GIT-2) used a full finite-element approach in their CFD/CSD simulations. Team members who used the modal analysis also may not have included all ten modes, as for example DLR who neglected the fifth flap and third lag modes since the weighting of these modes was observed to be two orders of magnitude less than their lower modal counterparts.

The BO105 model rotor blade is clamped at the rotor hub, and the hub stiffness from the center of the hub to the blade bolt ( $0 \leq y/R \leq 0.075$ ) is assumed to be very stiff compared to the remainder of the blade. The blade clamp outwardly adjacent to the blade bolt extends to  $0.099R$  and is also much stiffer than the airfoil portion of the rotor blade. Traveling radially outward, next is the flexible blade root which extends to  $0.22R$ , the start of the airfoil portion of the blade. As realistic experimental data were not available in the region up to the  $0.22R$ , the partners have some freedom in the definition of stiffness in this area.

The axis for the center of gravity along the airfoil portion of the blade is aft of the elastic axis by almost  $9\%c$ . The center of gravity is located  $1.24\%c$  aft of the quarter-chord (where the aerodynamic loading was applied in the CFD/CSD coupling). These locations were obtained via structural analysis rather than experimental measurement.

The frequency diagram predicted by the CSD methods for the hingeless BO105 model rotor blade is shown in Fig. 3. The circles at 0% RPM represent the experimental data obtained for the nonrotating frame (Refs. 4, 61). Note that all four blade frequencies for the first torsion are plotted, but the CFD/CSD solutions should compare with blades 2 and 3, which have not been instrumented and match the structural blade descriptions used to build the computational models. At 100% RPM the sequence of modes from the lowest to the highest frequency were observed to be first lag, first flap, second flap, first torsion, second lag, third flap, fourth flap, second torsion, third lag and finally the fifth flap. As there were no experimental data, the quality of the data is evaluated by comparing to the mean of all partners' data. For these first ten modes, the individual error from the mean at the nominal 100% RPM varied no more than  $-2.1\%$  to  $3.05\%$ . These maximum deviations occurred at the second torsion mode, resulting in a difference of  $5.15\%$  between two partners. For the remainder of the modes, the deviation between partners' results was no more than  $3.15\%$  (second lag) and was equal or less than  $1\%$  for most of the flap modes. The scatter in the predictions was observed to increase overall as the nondimensional natural frequencies increased.

Important differences between the partners results occur for the two torsion modes, which vary from  $3.76$  (DYMORE4: GIT-1) to  $3.86$  (UMARC: UMD) for the first torsion mode and from  $10.43$  (S4: DLR) to  $10.99$  (CAM-RADII: AFDD-1, NL-1 and NL-2) for the second torsion

mode. These variations are a result of the different modeling approaches of the flex beam, where some users model the blade pitch attachment with a soft-in-torsion element at the blade bolt area or a free end with a torsional spring at this position. Both the element beam torsional stiffness and the spring stiffness are tuning factors that the partners used to tune their models to the nondimensional first torsion frequency of  $3.77$ , as predicted by DLR's S4 code. Thus, different spring stiffnesses ranging from  $1,000$  Nm/rad (GIT-2) to  $2,336$  Nm/rad (UMARC) have been reported for each structural model in this effort. The spring stiffness for the experiment is reported as  $400$  Nm/rad (Ref. 4).

At 100% RPM the dominant components of the first five flap, three lead-lag, and two torsion mode shapes were examined, as reported in Figs. 5, 6, and 7. The partner results in Fig. 5 indicate excellent agreement across the methodologies applied, in particular for the lower modes. The partners' predicted mode shapes compare very accurately to one another as the computed natural frequencies also closely align (Figs. 3 and 4). As the higher modes do not contribute significantly to the total blade deflection, differences at the higher modes are less important. For example, as the blade tip deflection results primarily from the first three flap modes, the larger discrepancies between the partners' fourth and fifth flapping modes are of less concern than differences noted in the first three flap modes.

The lead-lag mode comparison (Fig. 6) is similar to that observed for the flap modes. With the exception of the AFDD-2 RCAS model, all results are virtually identical for the first two lead-lag modes. The third lag mode shows some minor differences due to phase shifts of the sinusoidal deflection, which again correlates to the larger scatter observed in the natural frequencies. During the simulations here and in Ref. 2, the first lead-lag mode dominates the blade motion with minor and negligible contributions from the second and third modes, respectively.

The torsional modes (Fig. 7) play a significant role in the blade dynamics, in part due to the closeness of the predicted mean first torsion natural frequency of  $3.82/\text{rev}$  (Fig. 3) with the HHC forcing control frequency of  $3/\text{rev}$ . Scatter between the partners' natural frequency predictions for the first torsion mode fall between  $\pm 2\%$  of the mean prediction, but the highest scatter of all modes examined occurs for the second torsion mode ( $\pm 3\%$  difference from mean). The largest excursion is a difference of  $5.4\%$  for the second torsion. These are in part due to the different stiffnesses determined for spring constraint during the tuning process with the first torsional mode. As both torsional modes contribute to the blade behavior, in particular in response to the airloads associated with BVI, the spring stiffness plays a role in the behavior of CFD/CSD predictions.

Using DYMORE4, the sensitivity of the structural dynamics variables with the value of the pitch spring stiff-

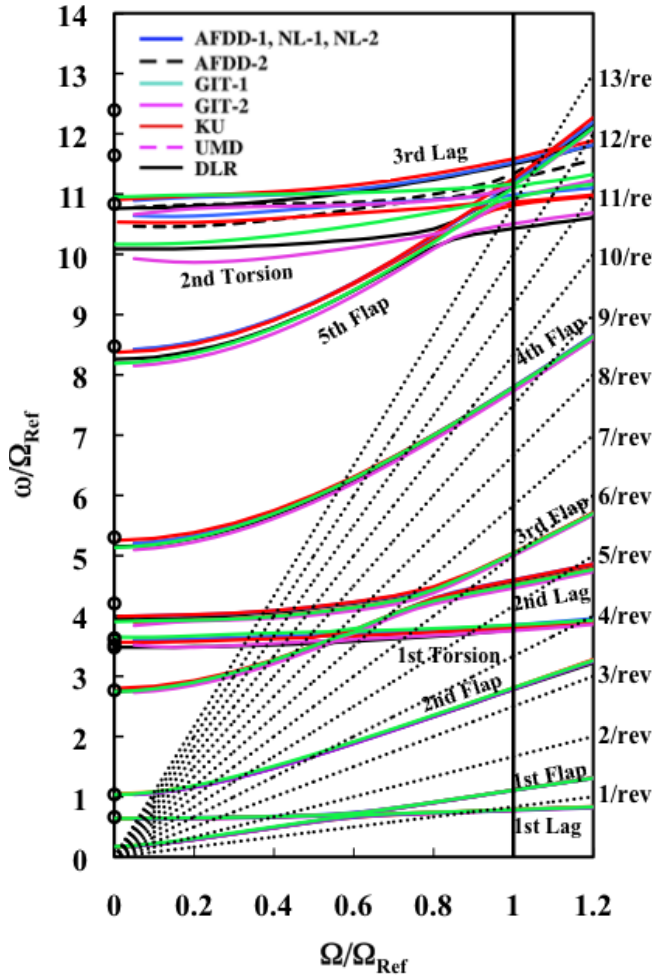


**Fig. 3. Frequency diagram of the BO105 model rotor predicted by the CSD methodologies**

ness was evaluated. For the flap and lead-lag modes, the differences between the natural frequencies at 100% RPM for two pitch spring stiffnesses of 1,600 Nm/rad and 1,200 Nm/rad lie within 0.0–0.3%. The differences of interest in the natural frequencies are observed for the first and second torsion modes at 3% and 1.5%, respectively. The higher spring stiffness resulted in equal or higher frequency values for all modes than the lower spring stiffness. The influence of the torsional spring stiffness was also observed in the mode shapes via small ( $\leq 0.2y/R$ ) shifts in the flap and lead-lag modes and slightly larger ( $\leq 0.5y/R$ ) for the torsion modes near the root. These differences are similar to, and fall within, the scatter obtained by the different partners' mode shapes in Figs. 5–7 and the natural frequencies at 100% RPM in Fig. 4.

### AEROELASTIC ANALYSIS

The aeroelastic, or CFD/CSD analysis, consisted of evaluation of the predictive trim, aerodynamic loads, deflections,

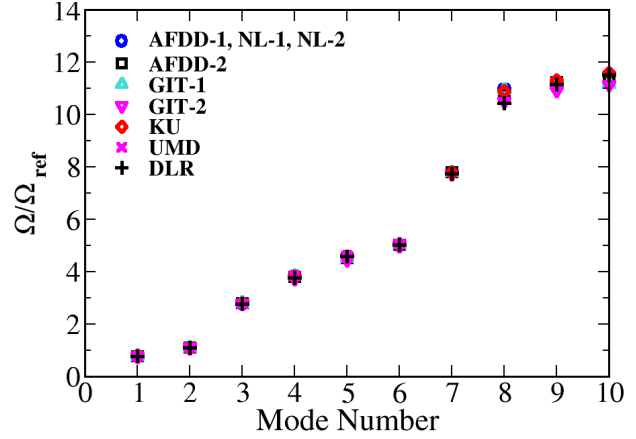


**Fig. 4. BO105 model rotor natural frequencies predicted at 100% RPM by the CSD methodologies**

moments, and wake capabilities of the methodologies. Due to the length of the analysis, aeroacoustic predictive analysis has been deferred to a separate document. Each of the assessed quantities is presented for all three of the cases evaluated: the baseline case (BL) that includes strong BVI, the HHC case optimized for minimum noise (MN), and the HHC case optimized for minimum vibration (MV).

These analyses include an aggregate of different investigations, some of which represent best practices by groups, and others which mimic one another to assess different aspects of the simulation. Specifically, these include:

- AFDD-1 and one of the NASA-Langley partners (NL-1) applied the same methods and CSD models, but using the best practices for grid generation and run simulation options within their organizations.
- Another NASA-Langley partner (NL-2) examined the impact of grid fidelity.
- One of the Georgia Tech partners (GIT-1) evaluated the influence of the structural modeling by keeping the CFD side of the simulation identical to that of the NASA-Langley partner (NL-2).
- A comprehensive code result that is a representative result from the best of the comprehensive predictions for the HART II rotor (Ref. 2) is included for comparison with that class of predictive methodologies.

In a more ad hoc manner, influences associated with methodologies (structured, unstructured, hybrid), turbulence models (one- and two-equations), and spatial and temporal integration are evaluated.

In this effort, comparisons are made for many of the variables with the means removed so that the simulations can be more easily compared. The mean adjustments for each variable are provided in Tables 7–9 so that the original data can be reconstructed.

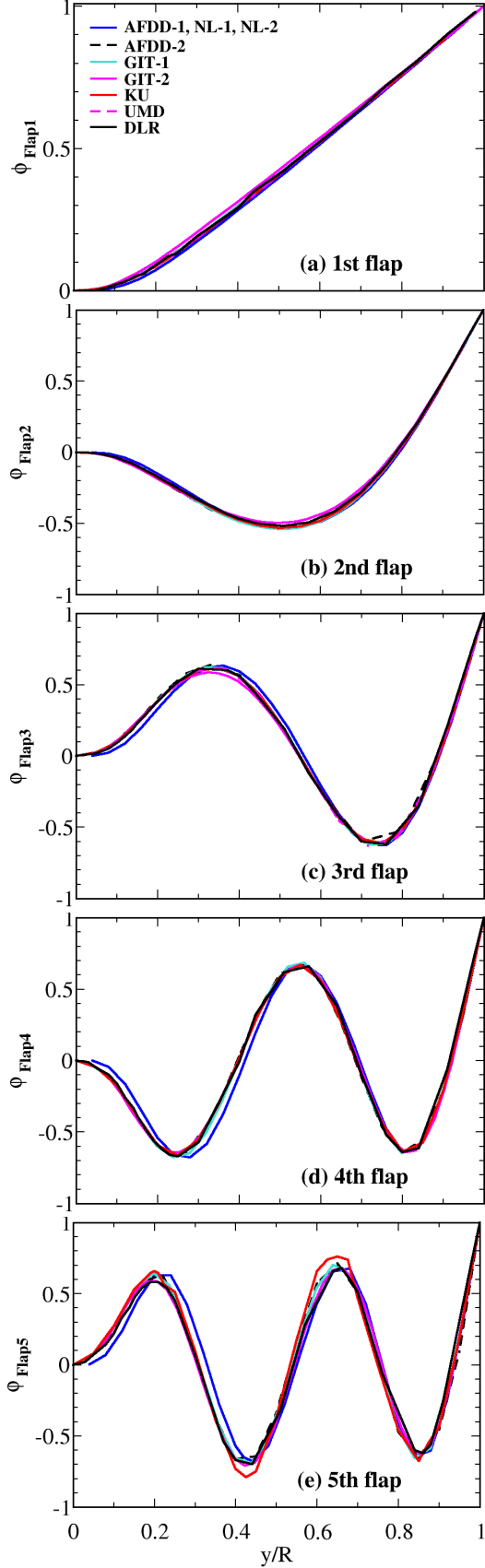


**Fig. 5. Flapping mode shapes predicted by the CSD methodologies**

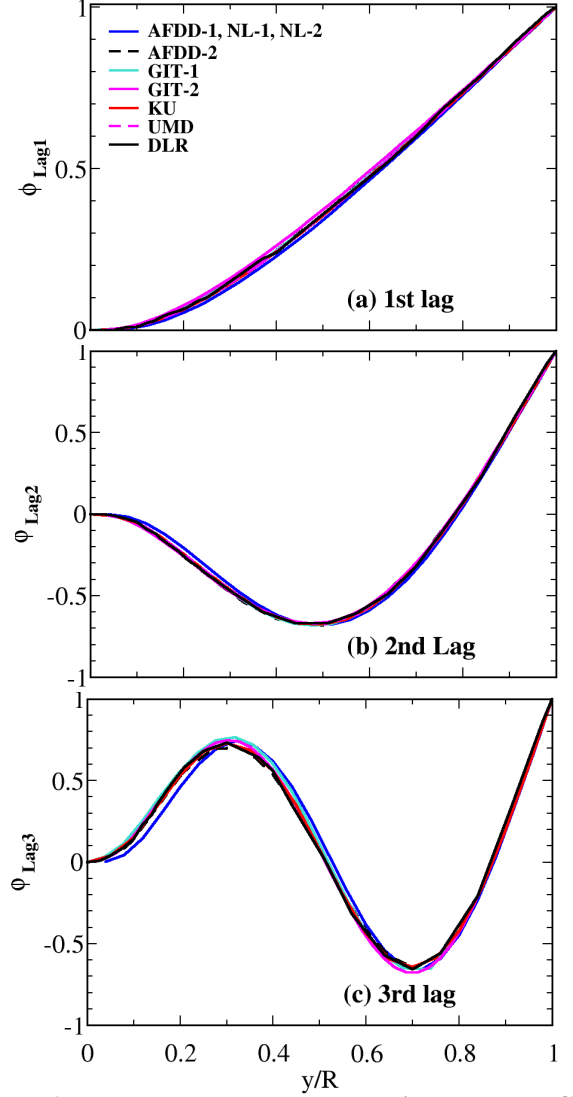


**Fig. 6. Lead-lag mode shapes predicted by the CSD methodologies**

In addition to the comparisons evaluated using rotor azimuth (time) as the independent variable, a statistical analysis of the data was also included to help assess the accuracy of the simulations. Bousman (Refs. 62, 63) introduced the method of correlating the slope and scatter of computations with experimental data to assess the overall accuracy. Figure 8 illustrates the concept of this analysis. The independent variable is the experiment data set, and a slope of one indicates perfect correlation with experiment. Consistent over/under prediction will have a slope greater/less than one. The slope should be used in conjunction with an assessment of the linear fit, which in this effort is the Pearson product moment correlation coefficient,  $r$ . The correlation coefficient is computed by dividing the covariance of two



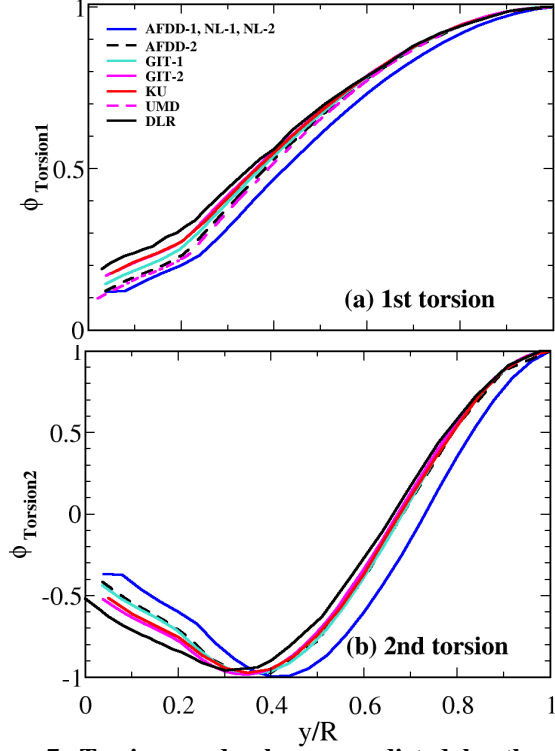


**Fig. 7. Torsion mode shapes predicted by the CSD methodologies**

variables by the product of their standard deviations:

$$r_1 = \frac{\sum(f_{cfd} - \bar{f}_{cfd})(g_{exp} - \bar{g}_{exp})}{\sqrt{\sum(f_{cfd} - \bar{f}_{cfd})^2 \sum(g_{exp} - \bar{g}_{exp})^2}} \quad (1)$$

where  $\bar{f}$  and  $\bar{g}$  are the independent and dependent variable means, respectively. For applications within this effort, the linear correlations are all positive, indicating that overall the simulations follow the direction of the data.

Rather than misusing the Pearson coefficient to indicate data scatter, the sample standard deviation,  $s$ , is computed for the residuals between experiment and computation, i.e.,

$$s = \sqrt{\sum[(f_{exp} - f_{cfd}) - (\bar{f}_{exp} - \bar{f}_{cfd})]^2} \quad (2)$$

where the barred quantity is the mean of the residuals. Here, the closer to zero that this positive quantity approaches, the less data scatter about the linear regression line is observed. If one assumes a normal distribution about the regression line (which may not be true), 68% of the data should lie within one standard deviation ( $\pm 1s$ ) and 95% of the data within two standard deviations ( $\pm 2s$ ).

As with all statistical analyses, the size of the sample space is important, so that the interpretation of the rotor aerodynamic loading where 360 computational samples are available is more accurate than the bending moments and tip

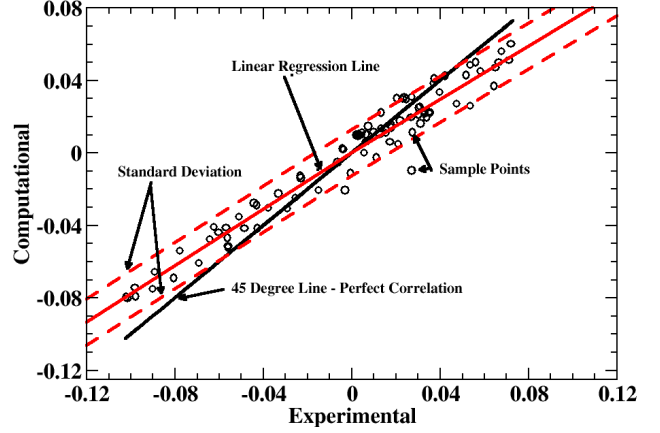


**Fig. 8. Example statistical correlation of computational variables with experimental data**

deflections where only 24 computational samples are available.<sup>2</sup> In addition, the presence of a few ‘outlier’ points is indicative of poor correlation of one or more features in the nonlinear data, which is not completely indicated in the linear statistical analysis. Given the quantity of data analyzed in this work, only the summary statisticals are presented and not the individual samples as seen in Fig. 8. These data are presented as two column plots, one which plots the difference between a perfect slope correlation (1) and the computational data (i.e., 1-computational slope), and a second which plots the value of one standard deviation of the error (experiment - computation). The reader is cautioned that these statistical data should be used in tandem with the time history data to provide an accurate analysis of the prediction methodologies.

## ROTOR TRIM

To evaluate the predictive capabilities of the codes, the rotors should be trimmed to the same operational conditions. As discussed previously, the structural dynamics analysis ensured that the rotor system was structurally modeled as closely as possible across the partners’ CSD methods, so that when the rotor is trimmed, the unknown variables associated with the computational aeroelastic modeling are further reduced.

During the experiment, the freestream velocity and rotor shaft angle were prescribed. From these, a shaft angle correction for the wind tunnel interference effects was extracted using the Heyson method (Ref. 64) and further

<sup>2</sup>The experimental data include 2,048 samples/rev for the aerodynamic loads and 256 samples/rev for the structural moments.

corrected using data from Brooks (unpublished; secondary citation in Ref. 65). These corrections resulted in a flow deflection of  $0.8^\circ$ ; so, an effective shaft angle of  $4.5^\circ$  relative to the freestream velocity was applied in the computational simulations rather than the experimental  $5.3^\circ$  shaft angle.

The experimental uncertainties associated with the measured forces and moments are 10 N and 10 Nm, respectively, based on the analysis of 32 revolutions of continuous measurements. These result in an uncertainty of  $0.01^\circ$  in the collective angle and  $0.04^\circ$  in the cyclic control angles.

As described in each partner's discussion regarding the simulation details, the CFD/CSD solution was run until the target trim parameters (thrust and roll/pitch hub moments) were achieved within some predetermined criteria. By using these criteria, the control angles and mean elastic twist were extracted when trim was reached. These values are portrayed as deltas from the experimental trim values in Fig. 9, with the corresponding experimental values given in Table 6.

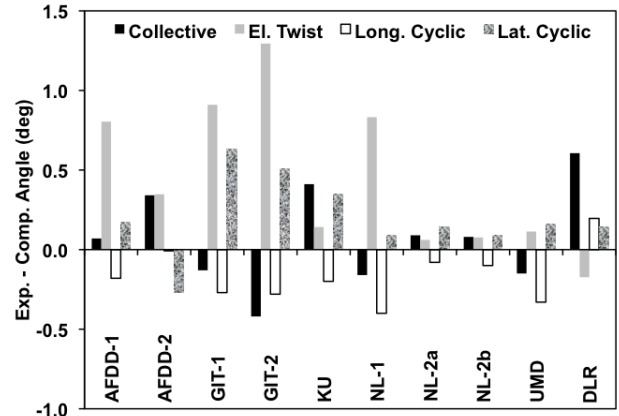
**Table 6. Experimental trim control angles and mean elastic twist**

Case	$\Theta_{75}$	$\Theta_{el}^a$	$\Theta_C$	$\Theta_S$
Baseline	$3.8^\circ$	$-1.09^\circ$	$1.92^\circ$	$-1.34^\circ$
Minimum Noise	$3.9^\circ$	$-1.17^\circ$	$2.00^\circ$	$-1.35^\circ$
Minimum Vibration	$3.8^\circ$	$-1.18^\circ$	$2.00^\circ$	$-1.51^\circ$

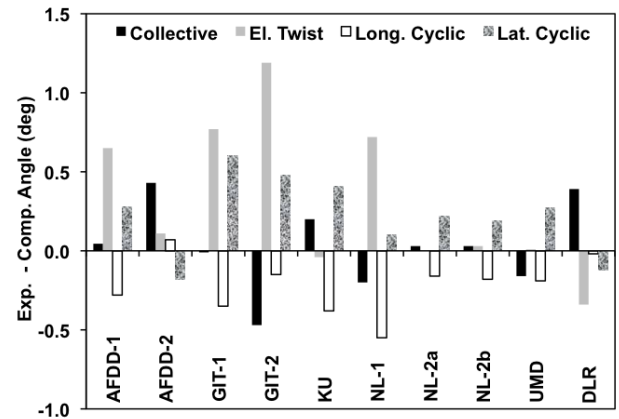
<sup>a</sup> Averaged over all four blades.

The control angles predicted by each partner are generally similar and in the majority within  $0.5^\circ$  of the experimental values. The mean elastic tip twist is somewhat larger for some cases, extending the difference up to  $\pm 1^\circ$ . In general, the CFD/CSD methodologies have the same tendency of over- or under-predicting a particular control angle for the same case. There is little difference between the trim angles when refining the grid (NL-2a and NL-2b), although larger differences are noted when the same methods are run with different grids/run options (AFDD-1 and NL-1) or different CSD methods (GIT-1 and NL-2a).

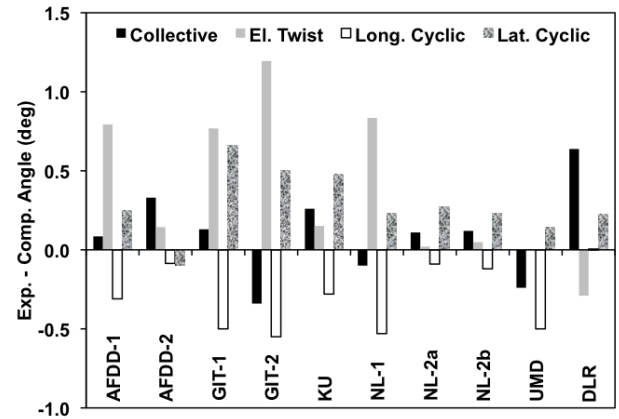
Since the collective angle and the mean elastic tip twist combine to provide the overall mean angle of the rotor, they can be examined as a sum (Fig. 10). The error associated with scatter of the individual blade motion extends the experimental data to  $2.4\text{--}3.1^\circ$ , as indicated by the red arrows overlaid on the experimental data. Only two sets of the CFD/CSD simulations fall within this scatter band (NL-2, UMD) for all cases, while the others fall below the experimental scatter range for one or more cases. This is primarily due to the larger negative mean tip twist predicted consistently by the CFD/CSD methods which tends to negate the closer collective angle predictions. The experimental mean elastic tip twist is based on an average of the deflections from all four blades.



(a) Baseline



(b) Minimum noise



(c) Minimum vibration

**Fig. 9. Rotor control angles and mean elastic tip twist at trimmed conditions relative to experimental values**

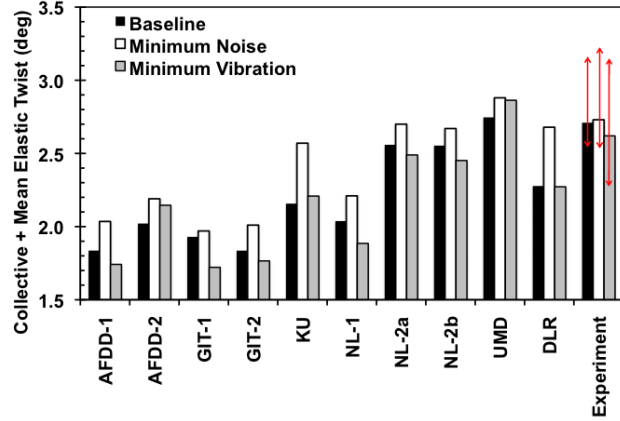


**Fig. 10. Sum of the collective angle and mean elastic tip twist**

There is no consistent trend to explain why some CFD/CSD methods fall within the scatter range and others do not. Turbulence modeling, temporal integration, computational structural dynamics method, etc., all show no distinct pattern from which to draw a conclusion. Van der Wall et al. (Ref. 2) suggest that the reason for this under prediction, which is also observed in many comprehensive methods, is that the velocity normal to the rotor disk is under predicted. This can be a result of either an under estimation of the wind tunnel blockage effects on the shaft angle, or that the influence of the wake on the rotor is under predicted by the simulations. This latter scenario implies that additional wake refinement may be necessary. For at least for the NL-2 study, which examined a baseline and a refined grid, additional grid refinement does not influence the outcome significantly since the baseline grid results (NL-2a) were within the experimental bounds of four rotor blades. Further numerical optimization studies, including wake refinement, may be warranted for the partner results that fell outside of the range.

## AERODYNAMIC LOADING

The aerodynamic loading was evaluated by examination of the sectional airloads at the 87% radial station where experimental data were obtained. The normal force and pitching moment coefficients have been normalized for compressibility effects by multiplication of the squared freestream Mach number,  $M^2$ . The experimental normal force and pitching moments were computed by integration of the 17 Kulite® pressures obtained along the 87% radial station. There has been a partial analysis to extract the differences associated with the integration of the BL aerodynamic loading with that of CFD simulation which includes hundreds of locations along each radial station (Ref. 55). For the normal forces ( $C_n M^2$ ), Boyd found that the effect of integration of

the full CFD resulted in a translational offset with the experimental data, but had little impact on the unsteady loading. His recommendation that these data be compared with experiment with the means removed has been adopted here. Differences for the pitching moment due to the integration patch, which was not examined in Ref. 55 may or may not be significant. Varying results have been observed through similar analyses of other configurations (Refs. 66, 67), in particular for separated flow conditions.

The capability of the computational methods to predict the aerodynamic loading has been assessed via two time history comparisons. The entire prediction (with means removed) are examined for one rotor revolution to assess overall trends. BVI events in the first and fourth quadrants of the rotor disk are also examined with the low-frequency content removed, allowing the high frequency content (11/rev and above) of the computations to be evaluated. While the experimental aerodynamic loading includes 2,048 data points for each rotor revolution, the computational data for each partner was gathered at  $1^\circ$  increments. To ensure that there is no bias introduced between the experiment and computations or between computations, all data were filtered identically at  $1^\circ$  increments. This leads to slight differences with the experimental data presented in Ref. 2, but maintains consistency for this comparison.

As discussed previously, only the reference blade, blade 1, was instrumented; and so, it resulted in a higher mean pitch and pitch oscillation magnitude compared to the remaining experimental rotor blades. A blade-to-blade difference was observed in the tip vortex strength for the experiment. This is not the case for the simulations, whose blades are all comparable. Thus, in addition to the influence of the pressure tap integration, the experimental data can have slightly higher means and magnitudes, although the latter is mitigated somewhat for the BVI events, which are caused by shed vorticity from all four blades.

**Normal Forces** The baseline case represents a descending flight where strong BVI occurs, in this case at azimuth angles of approximately  $50^\circ$  and  $300^\circ$ . For the minimum noise and minimum vibration cases, the BVI is significantly reduced or virtually eliminated at  $50^\circ$ . The normal forces (means removed) predicted by the CFD/CSD analyses appear to be overall comparable, as observed in Fig. 11, given the differences between grids, code algorithms, and structural models. The largest scatter between CFD/CSD predictions exists for the baseline case, which was expected due to the strong BVI.

For the baseline case, several features can be seen in Fig. 11(a). While the S4 comprehensive code anticipated by  $5-10^\circ$  the minimum loading (at  $160^\circ$ ) during the transition from the advancing to the retreating side of the rotor disk, the CFD/CSD methods lagged experiment by  $5^\circ$ . All

methods except DLR and UMD predicted the magnitude of the minimum loading within 0.01 of  $C_n M^2$ . Only the KU simulation predicted the sustained normal force plateau between an azimuth of  $70^\circ$  and  $120^\circ$ . The GIT-1 prediction had the smallest magnitudes for the main BVI events in the first quadrant, as well as a under prediction of the loading from  $0^\circ$  to  $40^\circ$ .

For the minimum noise case (Fig. 11(b)), the overall predictions appear to be more consistent with one another and more accurate when compared to the experimental data. The full CFD/CSD and comprehensive methods except for GIT-2 predict the phase and magnitude of the normal force very well. Moderate overshoots in the peaks of 0.01-0.03  $C_n M^2$  are observed for some of the methods. The hybrid methods (GIT-2, UMD) show significant deviations in the magnitudes at various locations (though not coincidentally); and they, along with the DLR comprehensive code, show more sensitivity to the BVI event in the first quadrant. The large over-prediction of BVI peak by these simplified methods may be due to the lack of dissipation of the tip vortices that the full CFD methods encounter. In the hybrid and comprehensive methods, the tip vortex strength is maintained in the Lagrangian wake, with some empirical modeling to account for vortex aging. Dissipation in the hybrid methods will not occur until the vortex re-enters the RANS near-body blade grid. The vortex trajectory will also play a role in the aerodynamic response, and as the two hybrid models do not model the fuselage, this was examined. As will be shown later, however, the vortex tracks predicted by the computational methods, with and without fuselage models, are very similar.

All full CFD/CSD simulations for the minimum vibration normal force case (Fig. 11(c)) show consistent trends in both magnitude and phase. The peaks located about  $90^\circ$  and  $180^\circ$  are under predicted by 0.01–0.02, but the phase is predicted within  $\pm 2^\circ$ . The hybrid simulations indicate that the magnitude of unsteady loading over a rotor revolution is under predicted. This is particularly evident at the  $140^\circ$  minimum loading location, where they under predict the amplitude by 0.04-0.05. This under prediction could be an influence of the fuselage, as the DLR comprehensive method with the fuselage is able to predict the extent of the loading. Lim et al. (Ref. 52) did not observe a similar change in the aerodynamic loading when using a full CFD/CSD (OVERFLOW/CAMRAD II) method with and without the fuselage.

Due to the number of CFD/CSD participants (10), the data plots are expanded to examine the BVI events (or the mitigation of these events) in the first BL quadrant.

Lim et al. (Ref. 52) noted that for their full CFD/CSD method, the influence of the fuselage was to increase the magnitude of the BVI events in the first quadrant, but there were only minor changes in the BVI predictions in the

fourth quadrant. Interestingly, all of the unstructured methods, to some degree, appear to be less influenced by the fuselage in the first quadrant, most dramatically for the BL case (Fig. 12). AFDD-2 is the least affected, while GIT-1, which uses the same grid and CFD code, but a different CSD method than NL-2a, is the most affected. The grid refinement in NL-2b from 14 to 23 million grid nodes improves the predictions after  $50^\circ$ , but has little effect in the oscillatory loading prior to  $50^\circ$ . Computations were undertaken for the GIT-1 case varying the pitch spring stiffness (increase by 400 Nm/rad) and modifying the number of subiterations with little discernable change in the predictions for this region. All of the structured methods applied higher-order spatial algorithms compared to the unstructured methods, which are limited to second-order accuracy.

For the MN and MV cases, the differences manifest themselves in a smoother loading increase between  $50^\circ$ – $90^\circ$  when compared to experiment and their structured full CFD/CSD counterparts. These differences between structured and unstructured methodologies were not observed for the fourth quadrant, which agrees with the minor influence of the fuselage observed by Lim et al. (Ref. 52). These observations and additional computations suggest that the grid may need to be refined in this area between the fuselage and rotor to capture these effects with the second-order spatial schemes. The numerical aspect of the simulation is recommended for further evaluation.

The low-frequency content of the normal forces has been removed, allowing the high frequency content (11/rev and higher) of the computations to be assessed. Expanding the high-frequency content of normal forces in the first quadrant (Fig. 13) highlights the differences between the simulations and with experiment. Experimental data indicate two BL BVI events at  $45^\circ$  and  $56^\circ$ , one MN BVI event at  $70^\circ$  and three weaker MV BVI events at  $40^\circ$ ,  $48^\circ$ , and  $58^\circ$ . Overall, the full structured CFD/CSD methods capture the 80% or more of the amplitude of the BVI events, but encounter phase shifts of up to  $6^\circ$ . The unstructured meshes have mixed success with capturing the amplitudes from AFDD-2 (60–80%) to the NL-2a/GIT-1 coarse mesh predictions (50% or less). The phase shift observed with the unstructured methods are comparable to or better than their structure method counterparts. The GIT-2 hybrid results generally over predict the BVI amplitudes, except for the strong MN BVI event which is under predicted. The other hybrid method, UMD, indicates mixed success for the amplitude predictions. For the BL and MV cases, the hybrid and comprehensive methods are marked by additional large events beyond  $60^\circ$ , which is indicative of higher elastic twist response, as discussed later. The single strong MN BVI event is predicted by the structured methods, albeit at reduced amplitude and up to a  $10^\circ$  phase shift. It is not predicted by the unstructured methods, indicating the im-



portance of the grid, as discussed previously. The phase of the multiple MV weaker BVI events prove to be the most difficult to predict in phase, and no conclusions between the various predictions can be drawn.

In the fourth quadrant, the dependence on full CFD/CSD variables appears less pronounced and comparisons with experiment are more favorable, as observed in Fig. 14. Overall the magnitude and phase of the BVI events are well-predicted, within 0.01 and  $\pm 2-4^\circ$  by the full CFD/CSD partners. The DLR (S4) comprehensive method overall predicts the phase of BVI events well, with an over prediction of the peak (within 0.03) of multiple BVI events but with good phase predictions. The hybrid methods miss some of the BVI phase predictions by up to  $10^\circ$  (GIT-2, lag; UMD, lead). Their magnitudes, once corrected for these phase differences, correlate relatively well with the full CFD/CSD predictions. These phase differences may be due possibly to the missing influence of the fuselage, which is included in the comprehensive solution (DLR). The DLR prediction, in addition to the full CFD/CSD methods, does not manifest the larger phase shifts observed by the hybrid methods without the fuselage.

The visual inspection of the prediction time histories can be augmented with statistical analysis to aid in evaluation of the predictions compared with experimental data. This quantitative analysis examines the deviation of the computational predictions with the experimental data. This is evaluated by plotting the experimental data as the independent variable and the computational data as the dependent variable. A slope of 1.0, combined with a Pearson coefficient ( $r$ ) of 1.0 indicates perfect linear correlation with experiment.

The statistical analysis of the normal force coefficient residuals in Fig. 15 shows some interesting trends. The correlations are above  $r = 0.84$  for all methods and cases (not shown), implying a strong linear correlation. The slopes are primarily within 5%-10% for the baseline case, with the exceptions of GIT-1, UMD, and DLR (comprehensive code). The standard deviation indicates the presence of some large excursions. For example, while GIT-2 has one of the most accurate slopes, it also has the largest standard deviation, indicating that the data have phase differences, so that an error band of 0.02 must be used to ensure that 68% of the predictions fall within this band. Conversely, GIT-1 has a larger slope deviation, but 68% of the predicted values lie within 0.01 (and 95% lie within 0.02) of the experimental  $C_n M^2$  values. Examining these in conjunction with the time histories in Figs. 11, 13 and 13, the large scatter of GIT-2 is due to phase shifts in the BVI predictions, which are sometimes significant, while the higher slope deviation of GIT-1 is due to the (lack of) BVI predictions in the first quadrant. An analysis was undertaken to extract the phase shift from the data, for example, GIT-2, and re-examine the statistics. These yielded mixed results as methods exhibit

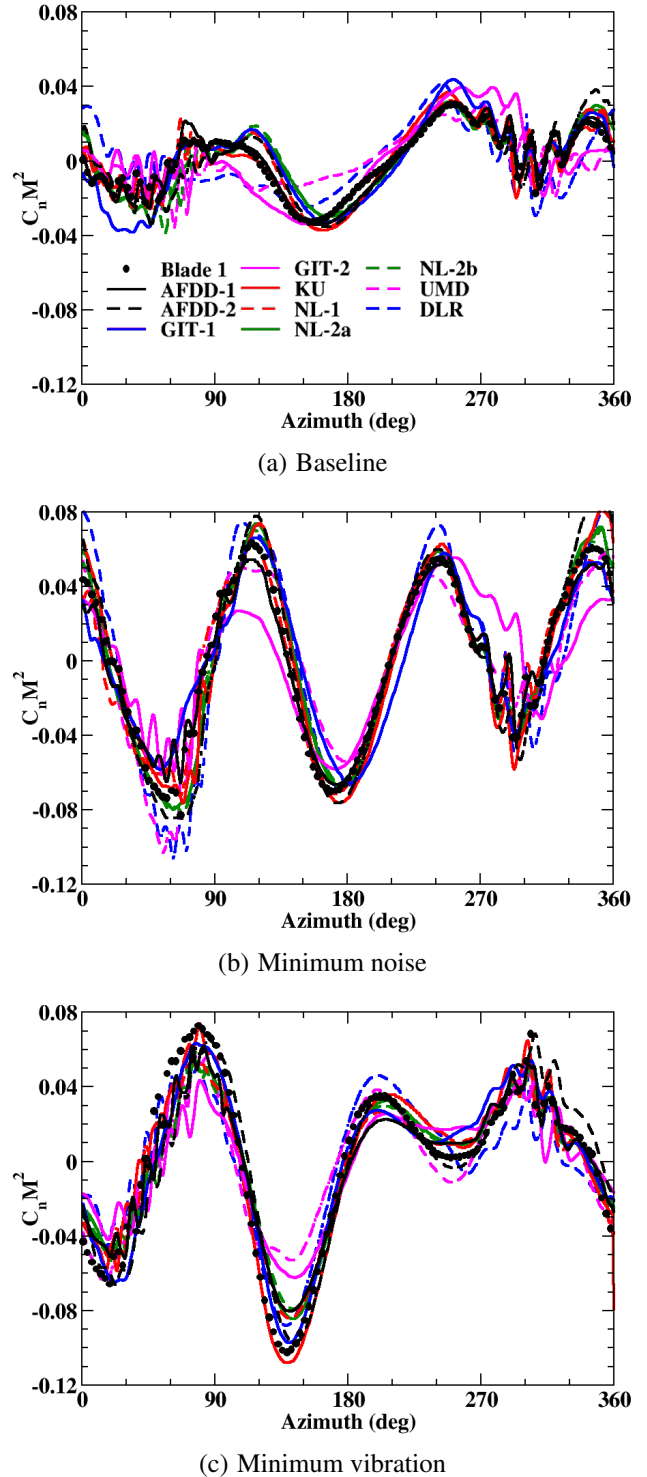


**Fig. 11. Normal force predictions at 87% radial station, means removed and normalized by  $M^2$**

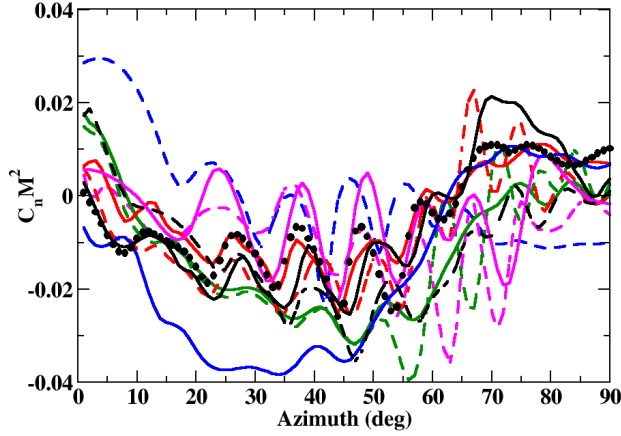


**Fig. 12. Comparison of the BL normal force predictions in the first rotor disk quadrant at 87% radial station, means removed and normalized by  $M^2$**

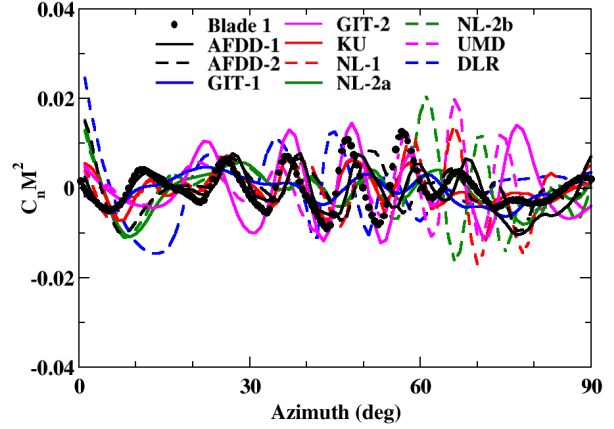
both positive (lead) and negative (lag) offsets in the phase prediction of both BVI and mean (low frequency) events. Thus, the statistical analysis includes all data, regardless of observed phase offsets, and the reader is again encouraged to use these statistical data in conjunction with the time histories.

Overall the KU simulation appears to be most statistically accurate of the methods with a relatively small error in the slope and the smallest scatter. Upon examination of Figs. 11, 13 and 13, it is apparent that this simulation captures many of the features with both small amplitude and phase error.

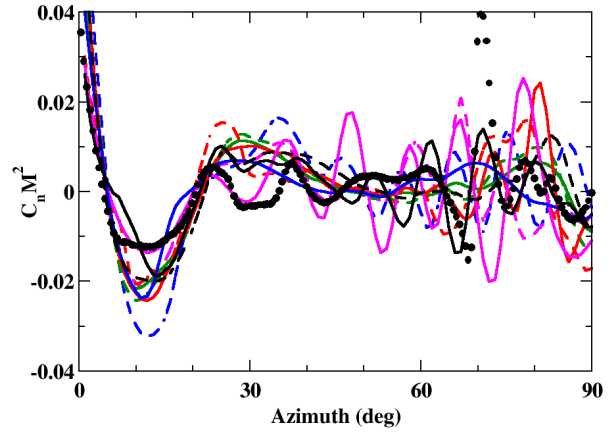
Similar observations can be drawn for the minimum noise and vibration cases, where, taken together with the scatter, the comparable methods are overall similar in their predictive accuracy of the normal force. The hybrid and comprehensive methods appear, in general, to have 50%-100% larger magnitude slope and standard deviations compared to the average of the full CFD/CSD results. Since the comprehensive method appears to be more statistically accurate than the hybrid methods, one may hypothesize that the lack of the fuselage may be a contributory factor.

**Pitching Moments** A similar analysis to the normal force was undertaken for the aerodynamic pitching moment for all three cases. The full revolution (Fig. 16), first quadrant high frequency (Fig. 17), and fourth quadrant high frequency (Fig. 18) pitching moments have been plotted using the same line definitions applied for the normal forces.

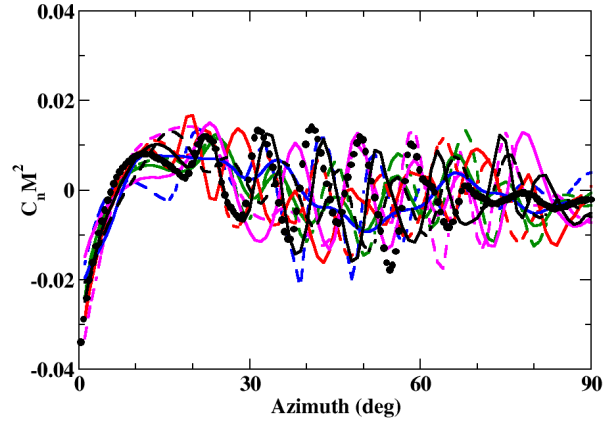
In general, for the full revolution (Fig. 16), the pitching moment appears to be similarly predicted by all methods, though the KU results do not capture the extent of the pitching moment recovery at about  $110^\circ$ , with a subsequent



(a) Baseline

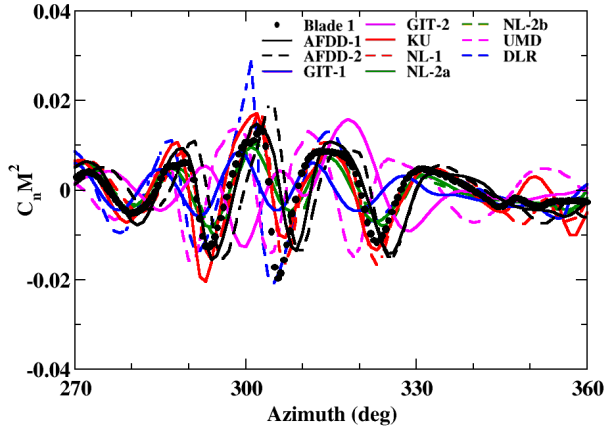


(b) Minimum noise

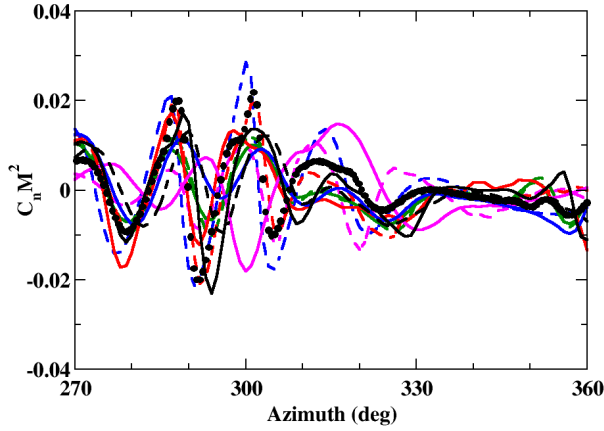


(c) Minimum vibration

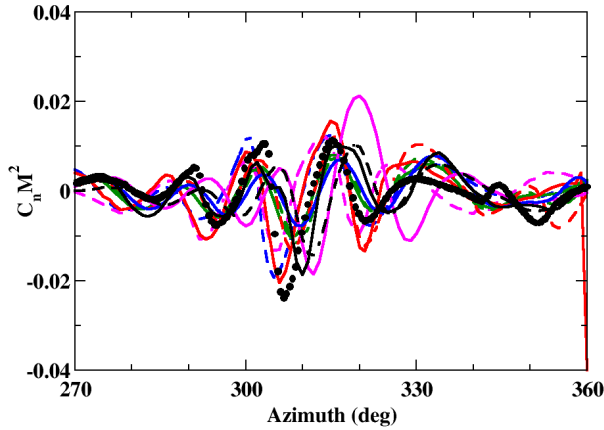
**Fig. 13. First quadrant normal force predictions at 87% radial station, means removed and normalized by  $M^2$**



(a) Baseline

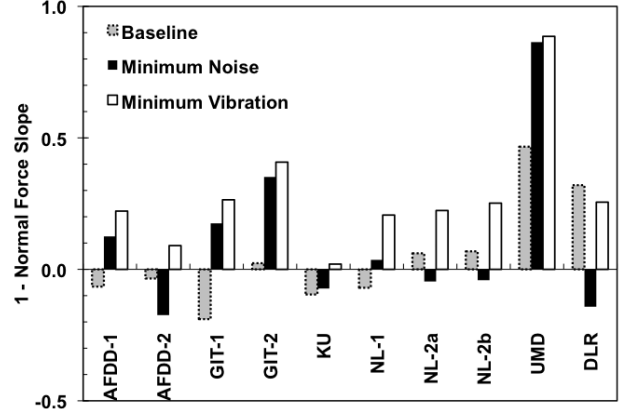


(b) Minimum noise

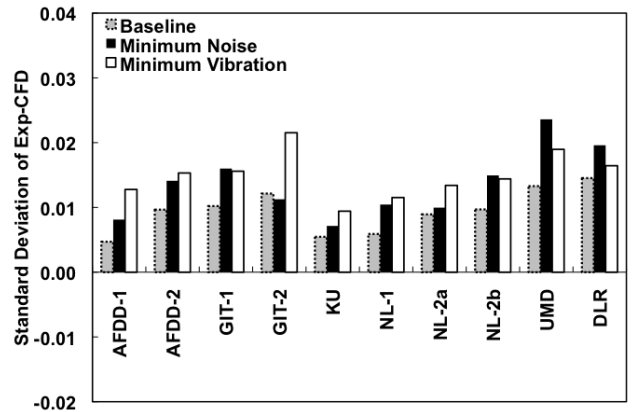


(c) Minimum vibration

**Fig. 14. Fourth quadrant normal force predictions at 87% radial station, means removed and normalized by  $M^2$**



(a) Normal force slope correlation



(b) Normal force error standard deviation

**Fig. 15. Sectional normal force residual statistical correlation at 87% radial station. Normal force coefficient has the means removed and normalized by  $M^2$**

translation offset until the recovery at  $190^\circ$  azimuth. Most of the methods, with exception of the GIT-1 results over predict the pitching moment about  $260^\circ$  by about  $0.0005$ – $0.001 C_m M^2$ .

Unlike the normal force, the methods do not align as accurately with one another for the minimum noise pitching moment. Most full CFD/CSD methods predict the behavior from  $100^\circ$  to  $260^\circ$  consistently, with overshoots at the pitching moment peaks at about  $135^\circ$  and  $260^\circ$ , but over predict the magnitude of the minimum moment at about  $190^\circ$  by  $0.0002$ – $0.0005$ . The phase of the minimum moment is well predicted with the exception of the KU that leads, and DLR and GIT-1 that lag the minimum by about  $10^\circ$ . KU's prediction has similar characteristics as its BL prediction, while the UMD, DLR and GIT-2 results equal or slightly under predict the magnitudes of the peaks, with varying phase lags.

The minimum vibration pitching moment is more con-

sistent, with similar differences observed for the KU, AFDD-2 and DLR results. The remainder of the methods fall within 0.0005 of the peak magnitude and  $\pm 5^\circ$  of the azimuthal location.

The expansion of the first quadrant pitching moments, including the removal of the low-frequency content (Fig. 17) illustrates that the overall levels in the baseline case are predicted within 5–10% by the full CFD/CSD methods, with a phase shift of approximately  $5\text{--}6^\circ$  of the BVI events. The characteristics of the methods in predicting the normal force remain relatively consistent here: under predictions by the unstructured methods and over predictions by the hybrid (GIT-2, UMD) methods for the same azimuthal regions. The comprehensive code tends to predict the pitching moments similar to many of the full CFD/CSD methods. This indicates the importance of the fuselage modeling when comparing to the hybrid results without the fuselage. The structured full CFD/CSD methods over predict slightly the magnitude of the oscillations. For most methods, the BVI reaction persists beyond  $60^\circ$  azimuth until  $90\text{--}120^\circ$ , depending on the method. The improved normal force correlation of KU with experiment compared to the rest of the computational methods for the baseline case is not readily apparent here.

The strong BVI event between  $65^\circ$  and  $90^\circ$  azimuth in the minimum noise case is predicted most accurately by the AFDD-1 simulation, which captures the sharp peaks and valleys, with little phase lag. The remainder of the full CFD/CSD methods capture only a portion of the BVI event, with residual oscillations between  $75^\circ$  to  $120^\circ$ . The GIT-2 and UMD hybrid methods over predict the oscillatory motion, while the DLR comprehensive method again is consistent with most full CFD/CSD methods.

For the first quadrant of the minimum vibration case where three weaker BVI events are located, the AFDD-1 accuracy observed for the MN case is not repeated; it and KU over predict the BVI amplitudes by a factor of about two, and includes a phase offset of about  $5^\circ$ . The remainder of the structured full CFD/CSD methods capture the magnitudes well, but the BVI peaks are  $0^\circ$  to  $180^\circ$  out of phase with experiment, depending on the method. Once again, the unstructured methods predict weaker BVI response, while the hybrid and comprehensive methods over predict the amplitude by a factor of 2–3, with phase offsets of  $0\text{--}10^\circ$ , which vary with method and BVI event.

In the fourth quadrant, the NL-1 predictions are overall the most accurate for the baseline case, though that is not true for the minimum noise and vibration cases. For all methods, there are features that are well predicted but others that are not, even within the same case. Overall, the levels and general features of the pitching moments exclusive of the BVI events are captured by all methods, although some (e.g., KU, UMD and GIT-2) exhibit large spurious oscilla-

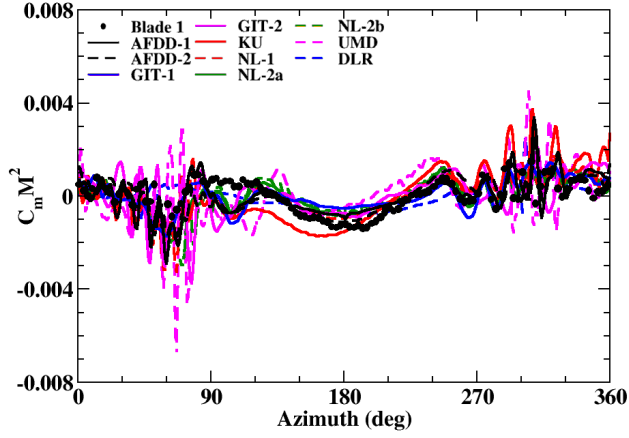
tions.

The statistical analysis of the pitching moment coefficient in Fig. 19 indicates some differences from the normal force analysis. The correlations are not as strong as the normal forces, remaining above 0.6 for all methods and cases, but still provide a relatively strong linear correlation. Unlike the normal force, where overall similar predictive behavior of each code was observed, there is widely varying capability of most methods across the three cases, as denoted by the differences in the slopes. The scatter is more consistent across each test case and most methods, with between  $0.005\text{--}0.001 C_m M^2$ . Comparing each test case, the hybrid methods (GIT-2, UMD) show less accurate correlation than their full CFD/CSD counterparts, and the comprehensive code (DLR) is overall comparable with the full CFD/CSD methods. The 64% increase in the grid density, likewise has no discernible influence on the statistical properties of the pitching moment. Application of the same CFD/CSD methodology, but using different grids and run properties indicates only differences in statistics (AFDD-1, NL-1). The influence of time step and/or turbulence is clearly apparent, in that the KU prediction, run at a stringent temporal integration, combined with a higher-order spatial scheme and two-equation turbulence model, shows a significant improvement in the slope correlation. This improvement has also been observed for hybrid RANS-LES turbulence methods run on refined grids and time steps for the UH-60A undergoing dynamic stall (Refs. 68, 69). The KU over prediction of the BVI events is clearly reflected in the scatter (standard deviation), which is comparable with the hybrid methods.

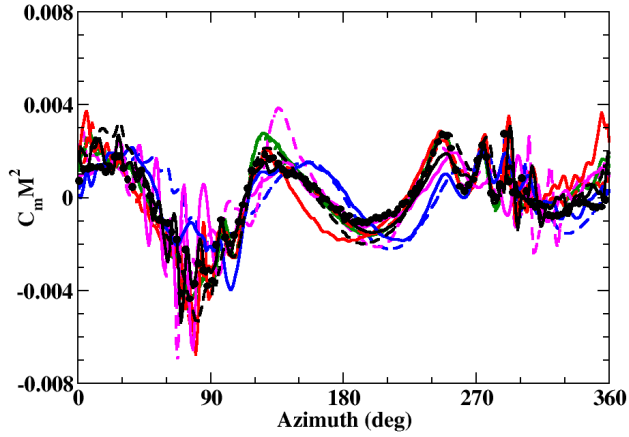
## BLADE TIP MOTIONS

The aerodynamic loading results in the elastic deflection of the rotor blades, which is examined next. The blade tip motion is defined in this effort as the elastic deflection without inclusion of, and relative to, rigid rotor motion and settings such as the pre-cone and pre-twist of the blade and the blade pitch control angles (including HHC for MN and MV cases). The tip deflection azimuthal time history has been selected to provide an assessment of the tip motions. During the experiment, the motion of all four blades were measured. Due to different instrumentation on each blade, the blades exhibit some differing motion, and the motion for all four blades is presented. Blade 1, the nominal reference blade, was found to always have an increased flapping and elastic twist compared to the other blades due to the presence of numerous pressure sensors which modified the elastic properties of the blade. The motion of blade 4 is similar to that of blade 1, as it also was fitted with pressure sensors, while blades 2 and 3 were not modified. These differences are reflected during the integrated properties of the rotor, such as thrust.

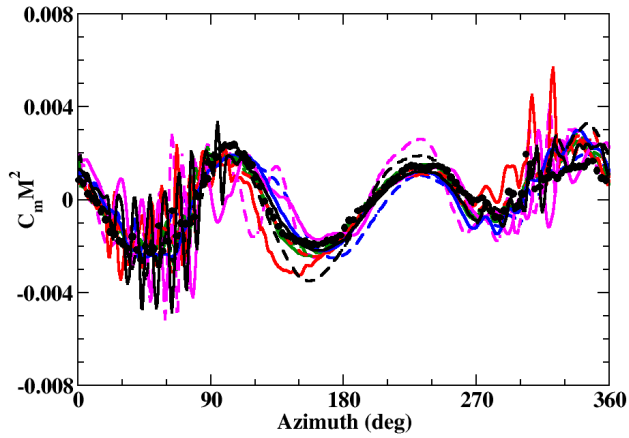




(a) Baseline

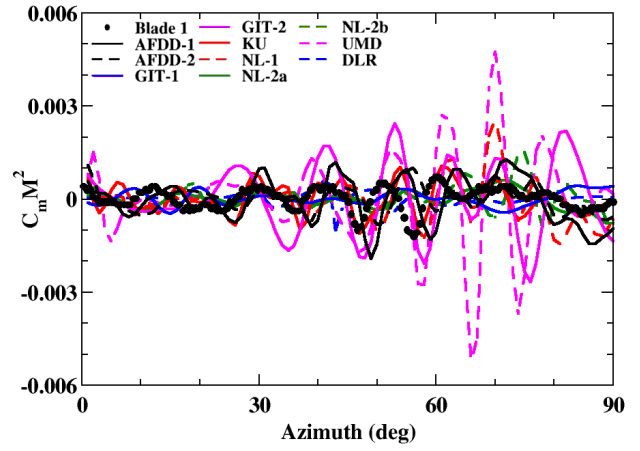


(b) Minimum noise

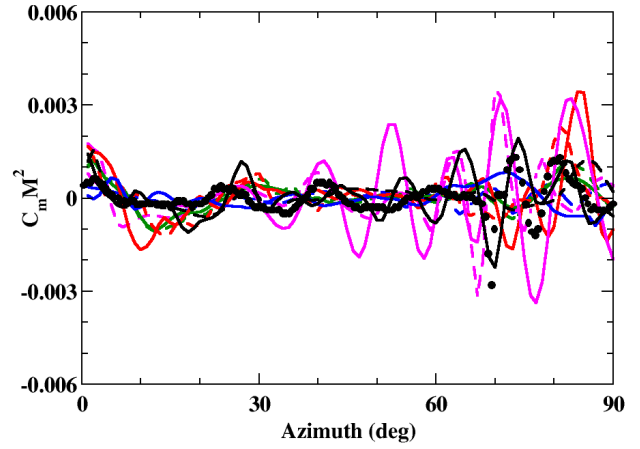


(c) Minimum vibration

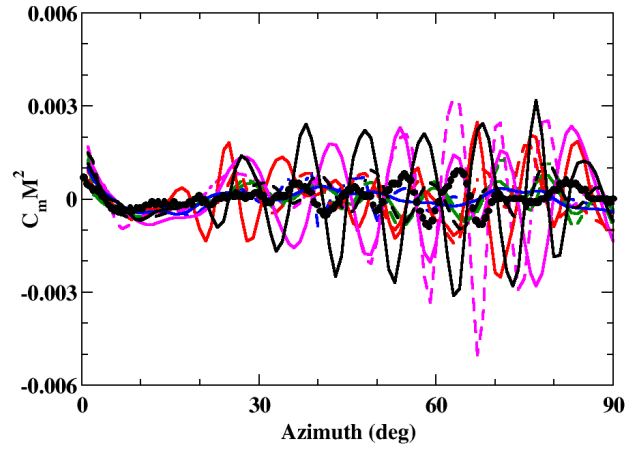
**Fig. 16. Pitching moment predictions at 87% radial station, means removed and normalized by  $M^2$**



(a) Baseline

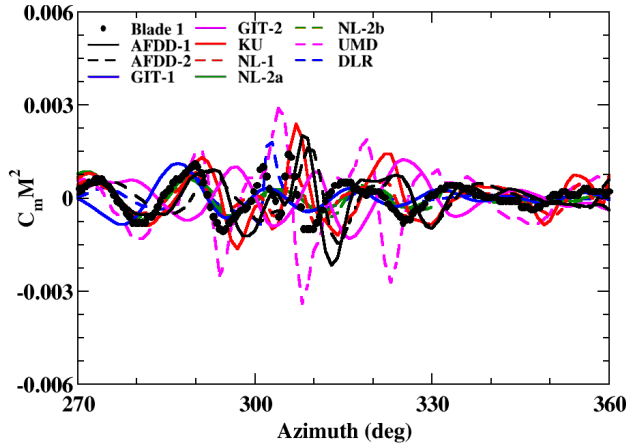


(b) Minimum noise

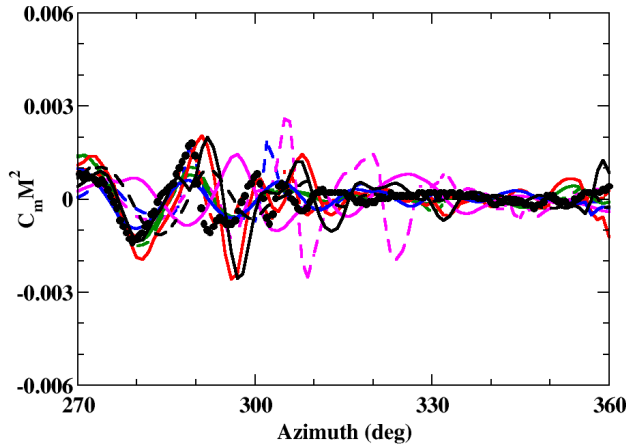


(c) Minimum vibration

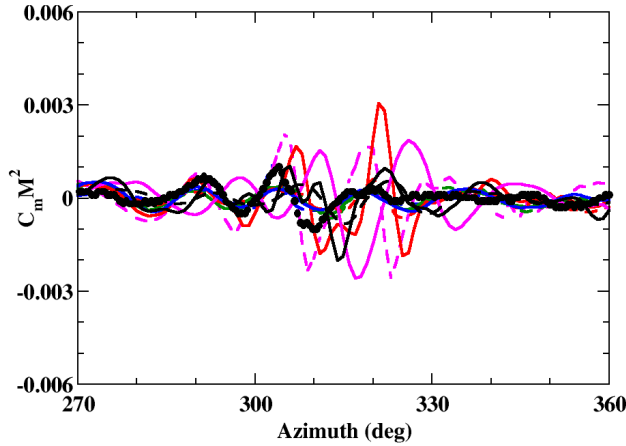
**Fig. 17. First quadrant pitching moment predictions at 87% radial station, means removed and normalized by  $M^2$**



(a) Baseline

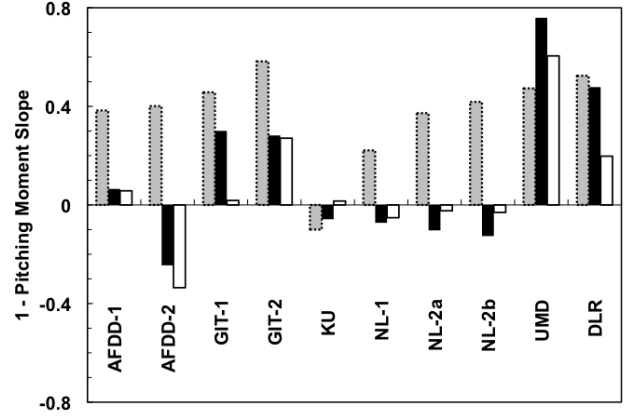


(b) Minimum noise

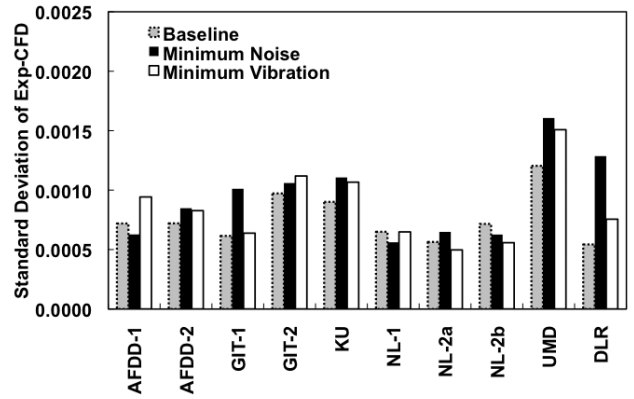


(c) Minimum vibration

**Fig. 18. Fourth quadrant pitching moment predictions at 87% radial station, means removed and normalized by  $M^2$**



(a) Pitching moment slope correlation



(b) Pitching moment error standard deviation

**Fig. 19. Sectional pitching moment residual statistical correlation at 87% radial station. Pitching moment coefficient has the means removed and normalized by  $M^2$**

The experimental data were recorded in increments of  $15^\circ$ , which was repeated for 100 revolutions and averaged. The measured tip blade motion including 6/rev components was synthesized from a Fourier analysis of the averaged signal using three flap modes, two lag modes and two torsion modes. These data have been shown to have an error within the accuracy of the original measured motion (Ref. 70).

Statistical analyses were again performed for the computational predictions. The data were reduced to  $15^\circ$  intervals or 24 samples per case, as this resolution is sufficient since only lower harmonics are present in the blade motion. The reduction in the number of samples results in a lower level of confidence than that for the aerodynamic loads analysis, but they are useful for revealing trends.

**Flap Deflection** The trimmed elastic flapping response for all cases examined is shown in Fig. 20. For all three cases examined, the flapping motion peaks between  $270^\circ$

and 280° azimuth and reaches a minimum between 80° and 100°. The minimum noise case also indicates the presence of a secondary elastic maximum at approximately 40–50°. Both the minimum noise and vibration cases have a saddle point about the 180° azimuth location.

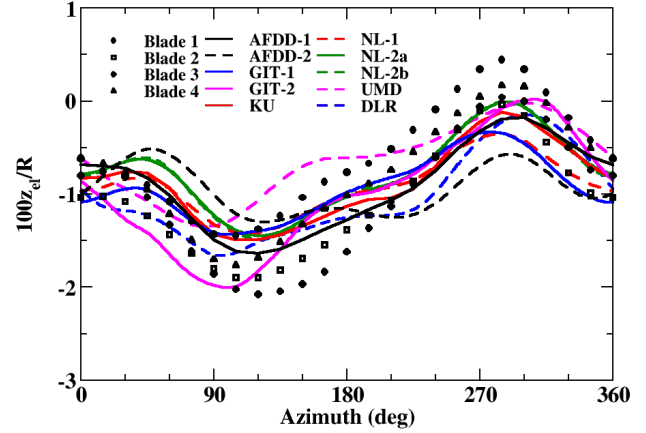
The full CFD/CSD simulations overall tend to predict the characteristics and phase of the flapping deflections. The scatter including all methods is on the order of 1–2 cm (0.5–1 ordinate units) or about 0.5 cm for most methods (excluding UMD, GIT-2 and AFDD-2), and results primarily from the differences in the amplitude predictions. The average scatter from the experiment varies between 0.55–0.65 cm, with maximums of up to 1.4 cm. The saddle points are predicted by all methods for the minimum vibration case and by all but AFDD-1 for the minimum noise case.

Statistically comparing to the motion of blade 1 (Fig. 21), the overall accuracies can be assessed over a full rotor revolution. The results across most predictions (AFDD-1, KU, NL-1, NL-2, UMD and DLR) are consistent, no matter which case is considered. Two of the unstructured methods (GIT-1 and AFDD-2) have some deviation with the experiment, which is due primarily to the phase shift observed in the time history data (Fig. 20).

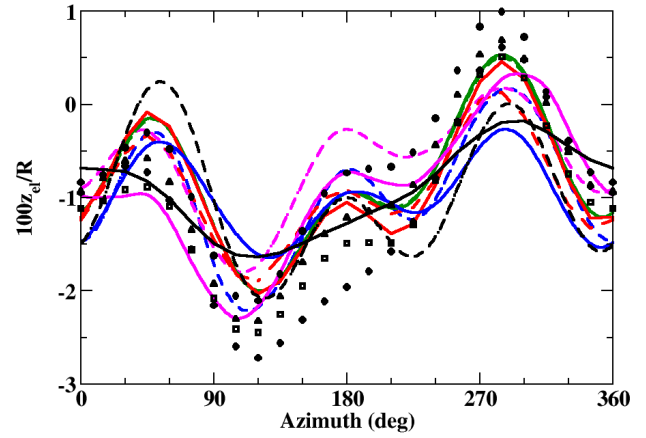
There is no indication that grid refinement improves the simulations (NL-2 cases are equal). The trend between the two partners running the same methodologies independently (NL-1 and AFDD-1) is inconclusive with respect to the slope accuracy but is consistent in the scatter. The methods are less accurate in predicting the minimum vibration and baseline cases compared to the minimum noise case. The CFD/CSD methods do not appear to have any advantage in predicting the flap motion compared to the less expensive comprehensive method (DLR). The lack of a fuselage model is not apparent in the accuracy of these predictions either.

**Lead-Lag Deflection** The lead-lag deflection is next evaluated, where  $x_{el}$  is defined as positive for deflections counter to the rotation direction, i.e., lag deflections. Comparisons of the computational simulations with experiment show a consistent translational offset of about 2–4 cm (0.57–1.14° lag angle), which was not able to be resolved during the HART II data analysis and is consistent with analyses of other computational methods of varying fidelity (Ref. 2). Thus, the means were removed for the analysis here. The mean values are listed in Tables 7, 8, and 9.

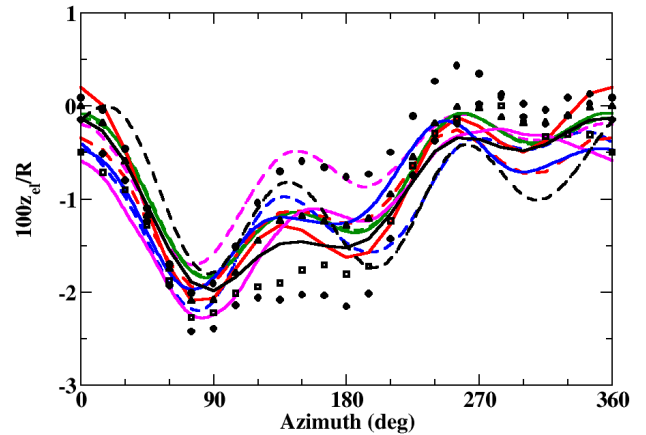
The in-plane tip deflections for all three cases result in a 1/rev motion that has its most forward location at 180° and reaches its most aft position at 0°, and these motions are impervious to the application of the 3/rev HHC in the minimum noise and vibration cases. Only minor differences between the CFD simulations and the experiment are observed for the tip lead-lag deflections in Fig. 22, with the



(a) Baseline

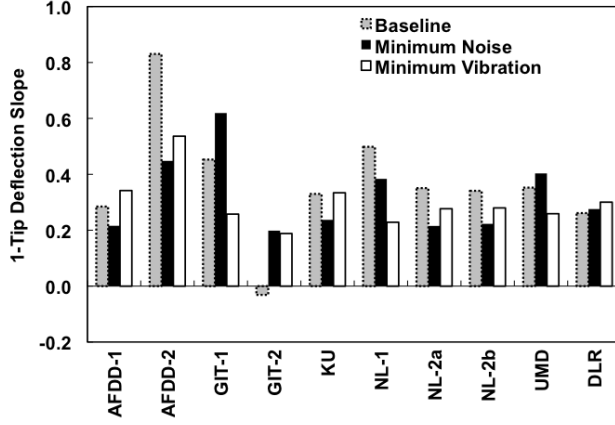


(b) Minimum noise

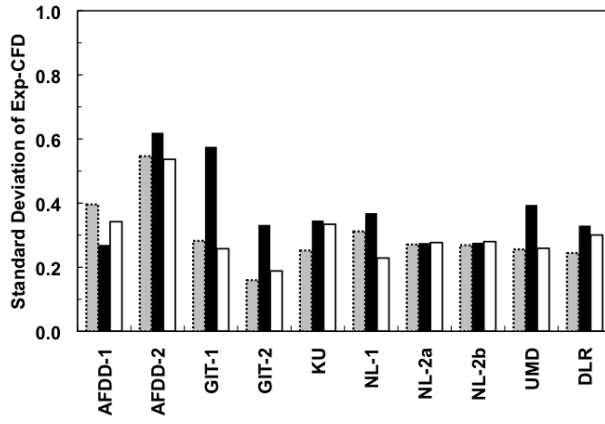


(c) Minimum vibration

Fig. 20. Blade tip flap deflections relative to pre-cone



(a) Deviation of the slope correlation



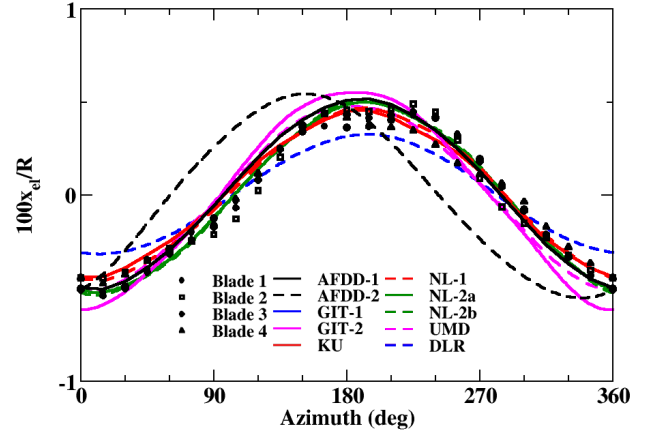
(b) Exp.-Comp. error standard deviation

**Fig. 21. Blade tip flap deflection residual statistical correlation relative to pre-cone**

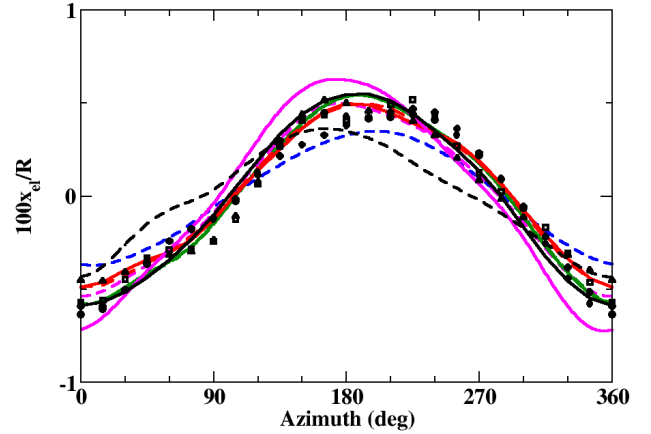
exception of the AFDD-2 simulations, which shows a phase lead of about  $10^\circ$ . The GIT-2 simulation also shows a similar phase shift forward of  $180^\circ$  maximum for the MN case. The differences between CFD/CSD coupling and the comprehensive analysis (DLR) is seen primarily in a reduction of the magnitude of the deflection predicted by the comprehensive code.

These phase offsets and magnitude reductions are reflected in the statistical analysis of the deflection residuals, shown in Fig. 23. The remainder of the CFD/CSD simulations have excellent correlation with experiment (typically within  $\pm 5\%$ ) for all cases, and the scatter is minimal, with differences of 0.1 or less.

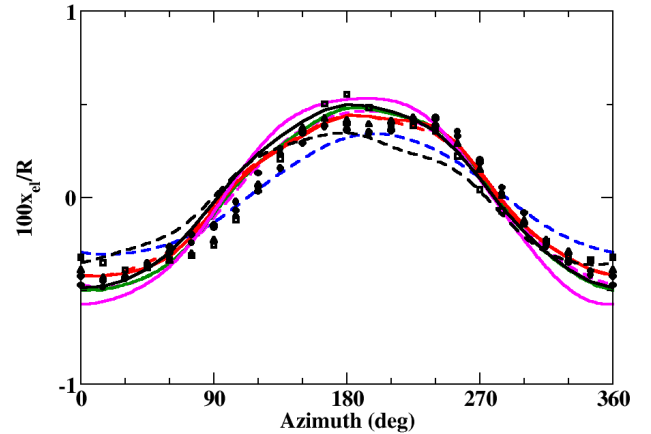
**Elastic Twist** The delay of the BVI events in the first quadrant observed in the aerodynamic loads (Figs. 13 and 17) can be in part correlated with the predicted behavior of the elastic twist (Fig. 24), where CFD/CSD predictions show a phase lag of the peak observed at  $90^\circ$  during the experi-



(a) Baseline



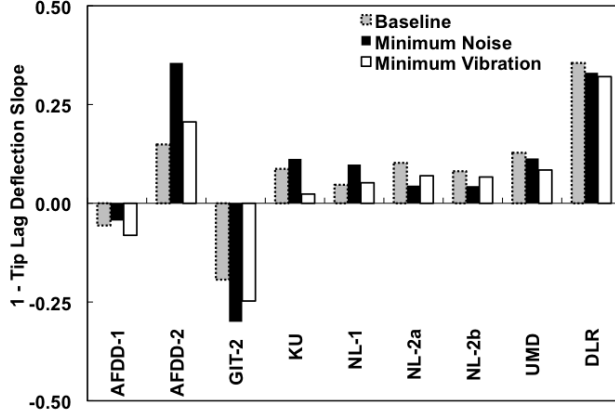
(b) Minimum noise



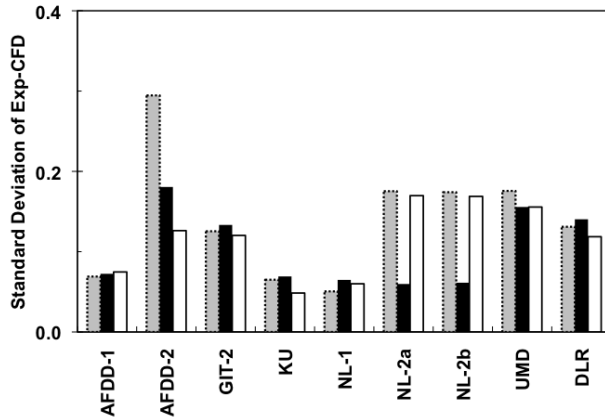
(c) Minimum vibration

**Fig. 22. Tip lead-lag deflection with means removed (Lag deflections are positive.)**





(a) Deviation of the slope correlation



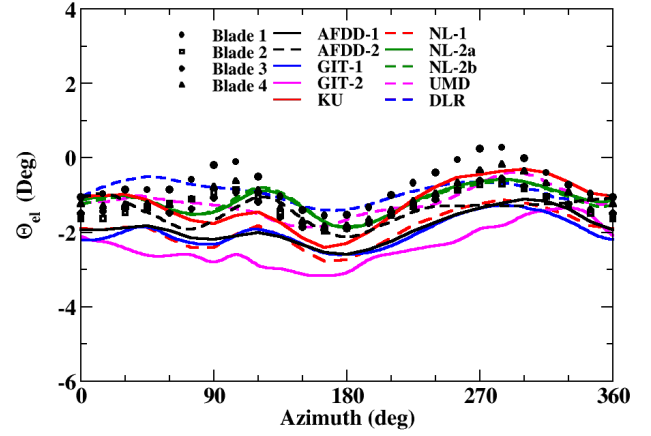
(b) Exp.-Comp. error standard deviation

**Fig. 23. Tip lead-lag deflection statistical correlation with means removed**

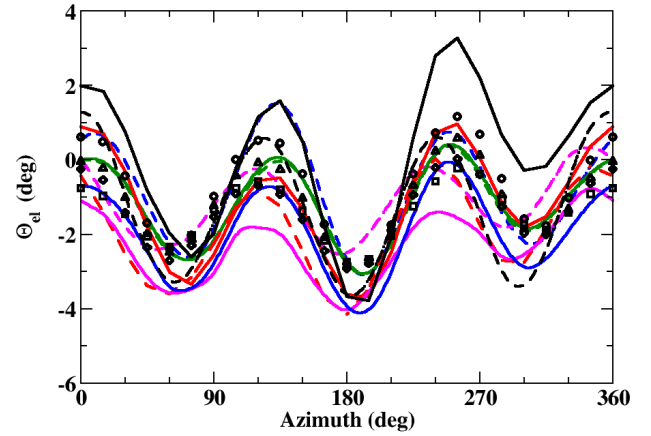
ment. While some partners' results predict the blade 1 twist levels at  $0^\circ$  quite well (NL-2, KU, UMD, AFDD-2), others (AFDD-1, NL-1, GIT-1, GIT-2) under predict the twist by approximately  $1^\circ$ . All partners except the two hybrid methods (GIT-2 and UMD) predict the 2/rev content of the baseline twist.

The 3/rev behavior of the elastic twist is generally predicted consistently by the different computational methods for the MV and MN cases. The GIT-2 simulation continues to have a translational offset and lower amplitude oscillations. The other hybrid method, UMD, tends to predict the magnitudes and mean of the elastic torsion more accurately than the GIT-2 hybrid method. The AFDD-1 simulation shows a translational offset of  $1.2^\circ$  and  $-1^\circ$  for the MN and MV cases, respectively, but captures the phases. These offsets do not appear to translate into a conclusive differential in the aerodynamic loading (Figs. 14 and 18) or, as will be seen, the torsional moments (Fig. 30).

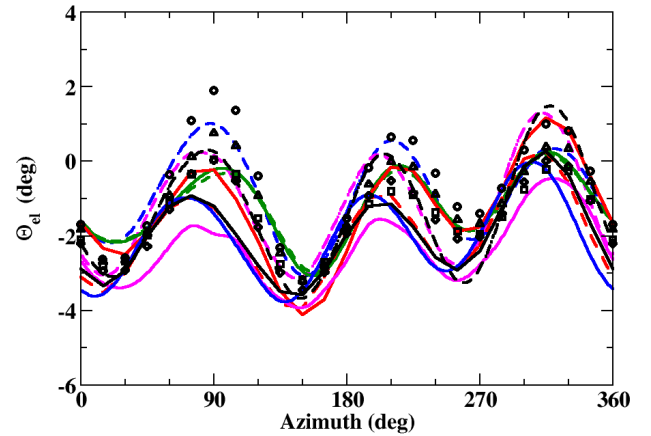
The statistics associated with the residuals of the elas-



(a) Baseline



(b) Minimum noise



(c) Minimum vibration

**Fig. 24. Blade tip elastic twist relative to the pre-twist and blade controls**

tic twist at the blade tip (Fig. 25) reflect the behavior observed in the time history plots. The large excursions noted for AFDD-2 and DLR in the baseline case, and AFDD-1 in the MN case are clearly reflected. Scatter varies from about  $0.4^\circ$  (one standard deviation) for the baseline case to almost double that value for some methods for the MV and MN cases. The correlation tends to be less positive for the elastic twist than for other variables, but this is not unexpected as the comparison is with blade 1, which is known to have a higher mean and larger elastic deformations, which is reflected in the comparisons.

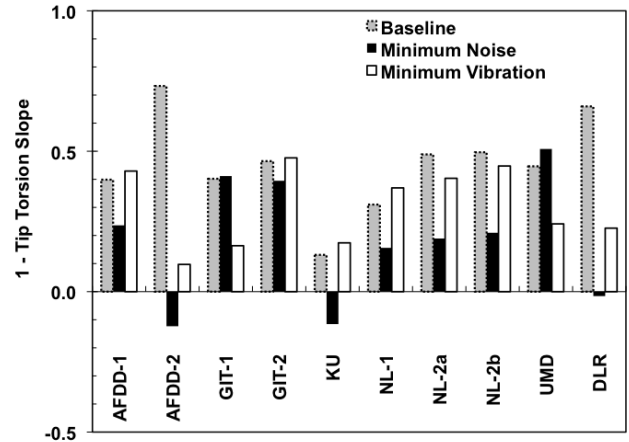
Once again, there appears to be little return for the increased grid refinement of the NL-2 computations. The difference in the OVERFLOW-CAMRADII runs by AFDD-1 and NL-1 indicate that the higher fidelity DES model and refined grid does not appear to have much benefit. While the CFD/CSD simulations provide a better prediction of the elastic twist for the baseline case, the same conclusion is not true for the MN case and in most instances for the MV case.

### Structural Moments

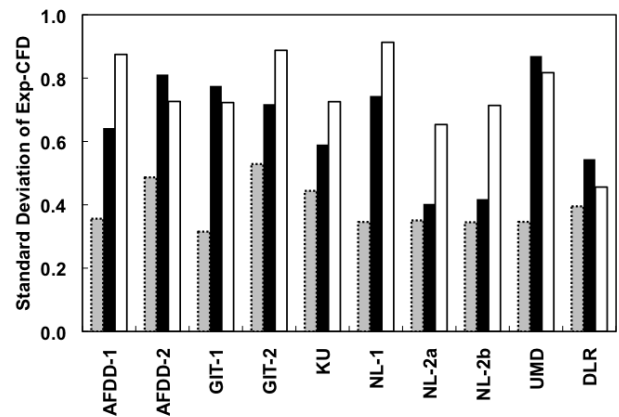
Strain gauges were placed on rotor blade 1 to measure the flap and lead-lag bending moments at  $17\%R$  and the torsion moment at  $33\%R$ . Only the dynamic (means removed) are compared as the strain gauge calibration was performed for the non-rotating system, and it is suspected that bias due to the centrifugal forces may cause a translational or mean offset. The data for the experimental were obtained by averaging the measured moments from 32 continuous revolutions.

The partners used two different approaches in computing the structural moments: the modal method and the force summation method. The modal method computes the bending moments (both transverse and in-plane) using the relation of the moment to the curvature (second derivative of the modal deflection multiplied by the bending stiffness) and the torsional moment using the relation of the moment to the twist change (first derivative of the modal twist multiplied by the torsional stiffness). Numerical errors associated with the computation of these derivatives may exacerbate the errors associated with the use of a few modes. The force summation integrates the forces radially outward from the reference location with its associated moment arm. While more computationally intensive, this approach tends to be more exact, in particular when a linear (modal) analysis is applied instead of the exact nonlinear representation of the structural dynamics of the rotor.

**Flap Bending Moments** The flap bending moments are examined at the radial station located at  $0.17R$  (from the hub center) where the largest curvature of the flap modes is observed (see for example, the fourth and fifth flap modes



(a) Deviation of the slope correlation



(b) Exp.-Comp. error standard deviation

**Fig. 25. Blade tip elastic twist residual statistical correlation with means removed**

in Fig. 5). van der Wall et al (Ref. 2) notes that for these HART II cases that comprehensive codes show a lack of correlation with the experiment, leading to unsatisfactory predictions of this parameter.

Figure 26 presents the CFD/CSD predictions of the flap bending moments for the  $17\%$  radial station. The 2/rev behavior of the flap bending moment is captured by most of the methods, albeit with large differences in both the amplitude and phase in some predictions.

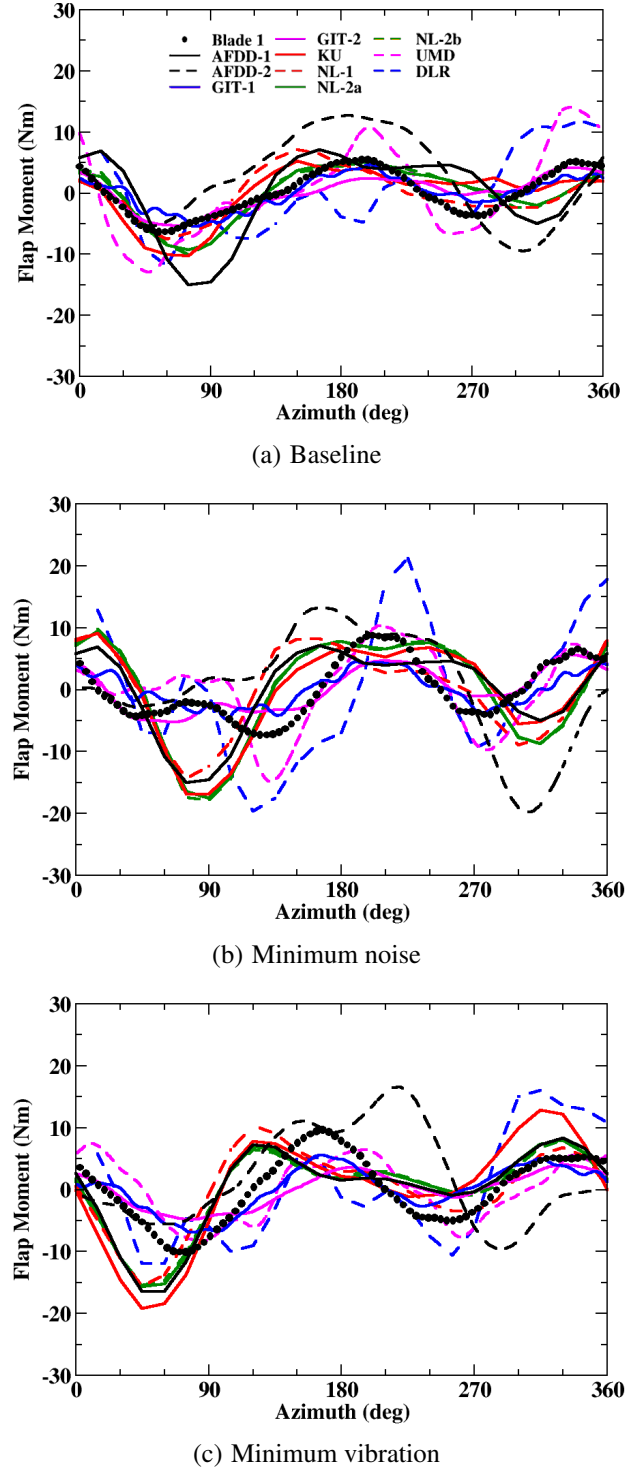
This does not carry over to the minimum noise and minimum vibration cases, where the two DYMORE-based (force summation) simulations appear to capture the behavior of flap bending moment more accurately in phase than the other models applying modal approximations. The observation cannot be applied to the RCAS (AFDD-2) simulations, however, which also applies the force summation method. The overall amplitude is under predicted. The modal-based simulations tend to over predict the bending moments with a  $20\text{--}30^\circ$  lead in phase.

Statistically in Fig. 27, it is clear that the CFD/CSD predictions for the flap bending moment have significant errors. On average, the slope correlation is in error by more than 30–40%, with some methods including scatter that is 30–40% of the amplitude of the moment. The less accurate prediction of the flap bending moment compared to the other parameters of interest merits further investigation.

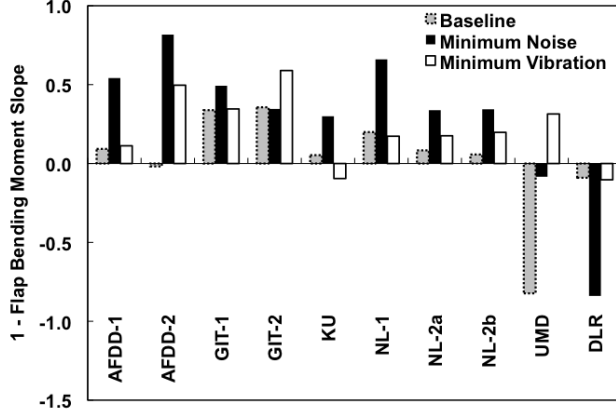
**Lag Bending Moments** The trend of the lag bending moments at 17% radial station is accurately predicted by the computational methods, as seen in Fig. 28 and clearly mimics the 1/rev motion in the lead-lag deflection (Fig. 22). This is true of the baseline, minimum vibration and noise cases. The maximum of the bending moments located between 90° and 270° is over predicted by the some of the computations up to 50%. The flattened plateau behavior is not predicted by the GIT-2 and UMD hybrid methods, but is predicted by the full CFD/CSD methods. For the minimum noise and minimum vibration cases, the AFDD-2 simulation is the most accurate, but it significantly over predicts the moment for the baseline case. The NL-1 and KU simulations consistently predict the trends most accurately for all the cases, followed closely by the NL-2 and AFDD-1 simulations. The grid refinement study of NL-2 shows no influence on this structural variable.

Figure 29 illustrates the scenario where the overall shape of a function is well predicted; but the amplitudes are, for the most part, over predicted. The over prediction of the amplitude of the lag bending moment is seen through the negative difference between the perfect fit (1) and the slope of the computational data. The standard deviation indicates the impact of this overshoot in amplitude. The largest overshoot (exempting the phase lag from AFDD-2) is seen to be GIT-2, which has an overshoot of 20–25 Nm, which is the amount shown in Fig. 29. Overall the best correlations appear to be the NL-1 and KU simulations, which combine higher fidelity turbulence modeling with small time steps.

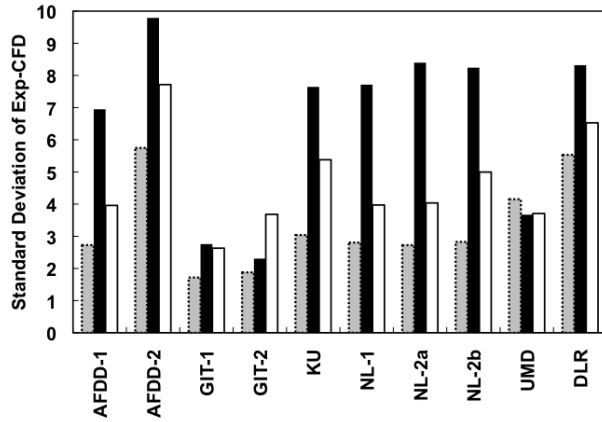
**Torsion Moments** The torsion moment is assessed at the 33% radial station where the second torsion mode reaches a minimum (Fig. 7). The torsion moments are shown in Fig. 30. As with the lag bending moment, the torsion moment is consistently predicted by the CFD/CSD methodologies. The overall amplitude of the torsion is predicted well for the baseline and minimum noise cases, and slightly under predicted in the minimum vibration case for most methods. There is a phase shift introduced by the GIT-2 hybrid method. There is minimal influence from the grid refinement, as observed by the superposition of the two NL-2a and NL-2b curves. The AFDD-2 simulation also shows some sensitivity to the minimum noise case, though the presence of a 10° phase lead, and a corresponding 40% decrease in the amplitude. This is not the circumstance in the



**Fig. 26. Flap bending moment predictions at 17% radial station with means removed**



(a) Delta of the slope correlation



(b) Exp.-Comp. error standard deviation

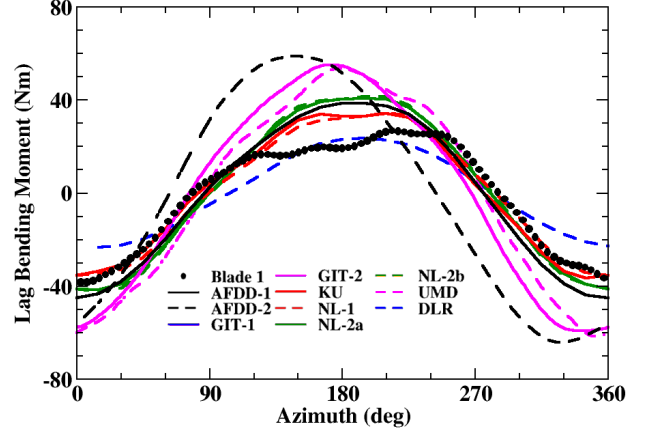
**Fig. 27. Flap bending moment statistical correlation at 17% radial station with means removed**

minimum vibration case.

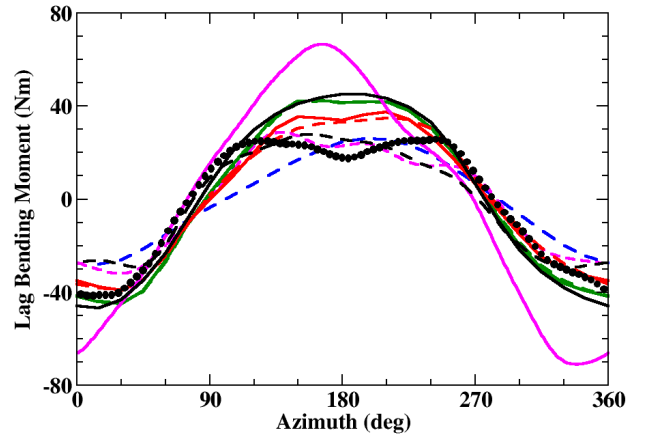
Statistically, the torsion moment has moderate correlation with experimental data as the slopes fall within 10–20% of the perfect correlation line. One standard deviation falls within 1 Nm for the baseline case and 2 Nm for the minimum noise and vibration cases. The grid refinement has a significant impact on the scatter when the NL-2a grid is refined to NL-2b for the HHC cases, though it does not have a significant influence for the baseline case. The comprehensive method has less success overall in correlating with experiment than its CFD/CSD counterparts, although the scatter remains approximately the same or better at 1 Nm for all cases.

## VORTEX LOCATIONS

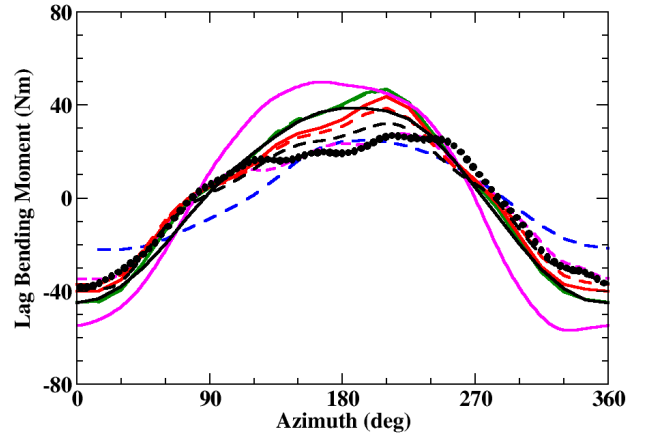
The vortex trajectories were measured experimentally at two blade azimuth location of 20° and 70° for a variety of radial stations. Here, data at the 70% lateral position



(a) Baseline



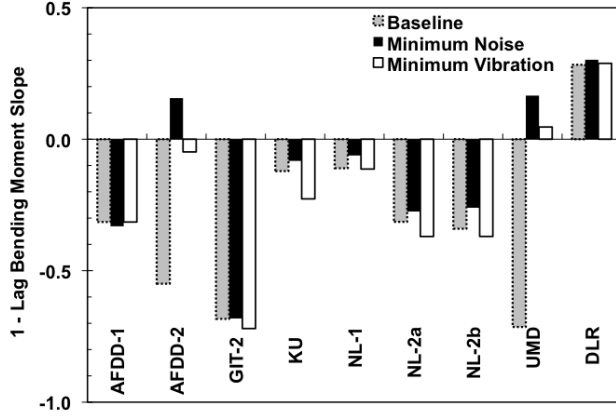
(b) Minimum noise



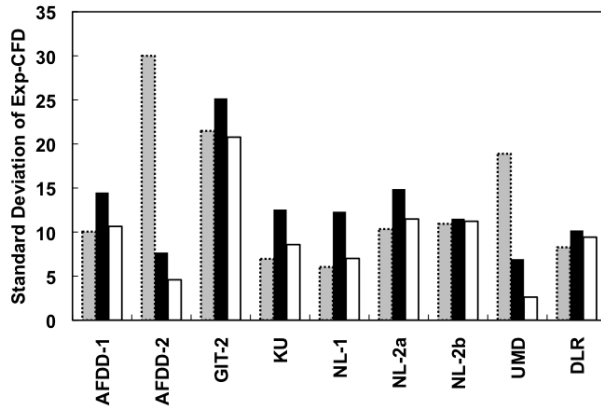
(c) Minimum vibration

**Fig. 28. Lag bending moment predictions at 17% radial station with means removed**





(a) Delta of the slope correlation



(b) Exp.-Comp. error standard deviation

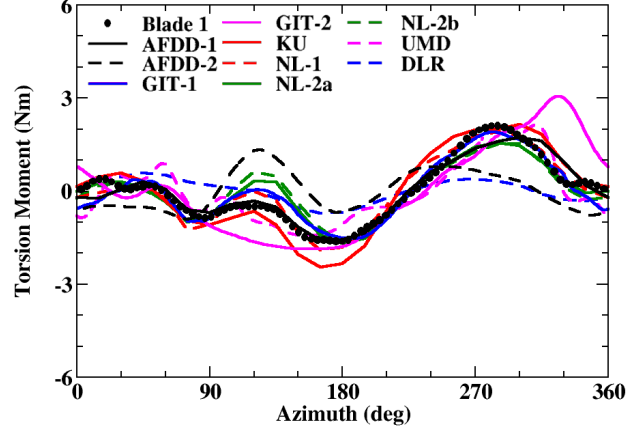
**Fig. 29. Lag bending moment statistical correlation at 17% radial station with means removed**

( $y = \pm 1.4m$ ), where BVI are encountered, are extracted from the CFD/CSD results, as well as from the comprehensive code (DLR), and compared with experiment. The experimental locations were computed from 100 vortex center positions isolated from PIV measurements.

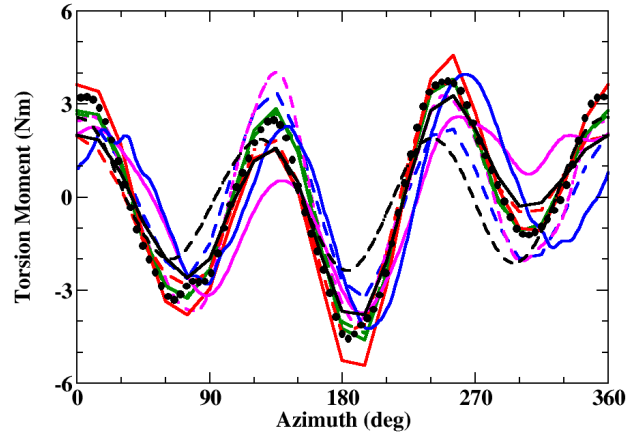
For the CFD/CSD simulations, the vortex locations were identified by the center of the location where the largest vorticity was observed. This was typically by visual inspection and interpolation of contour plots, such as the sample included as Fig. 32. Thus, there may be an additional error from this exercise with regard to the location of the vortices.

The NL-2 partner provided vortex locations for only NL-2a, as the two simulations appeared to have the same predicted vortex tracks.

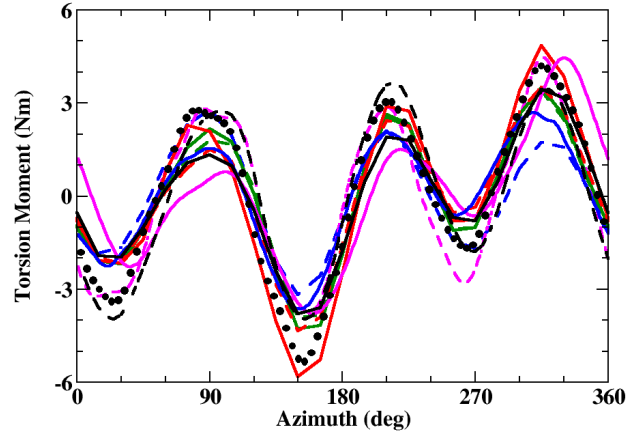
**Advancing side** The advancing side vortex positions are graphically illustrated in Fig. 33, where the experimental open symbol is the vertical position of the reference blade 1 at the reference position of about  $135^\circ$  azimuth. Since



(a) Baseline

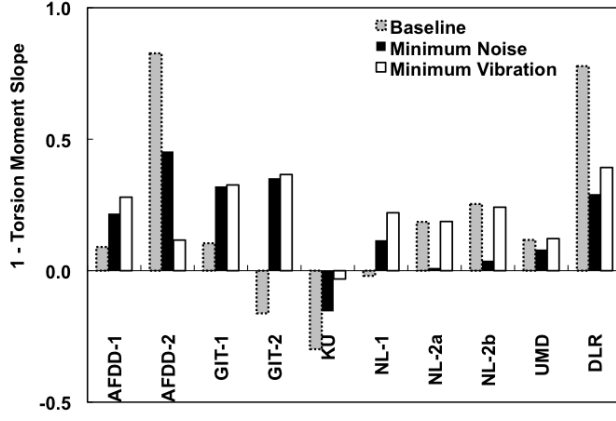


(b) Minimum noise

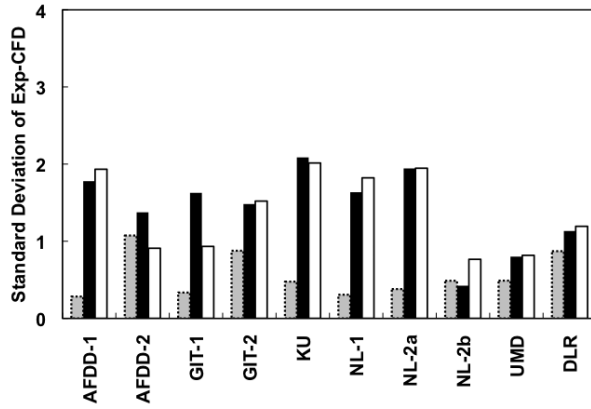


(c) Minimum vibration

**Fig. 30. Torsion moment predictions at 33% radial station with means removed**



(a) Delta of the slope correlation



(b) Exp.-Comp. error standard deviation

**Fig. 31. Torsion moment statistical correlation at 17% radial station with means removed**

the vortex positions were measured by using blade 1, which has higher mean flapping position than the other blades, the vortex position extracted from the computational results is expected to appear below that position.

This artifact is observed for all the computational results with the exception of the UMD predictions for all of the cases, and AFDD-1 for the MN case. The curved track of the vortex is predicted well by all methods except the GIT-1 simulations. The scatter is somewhat expected given the ad

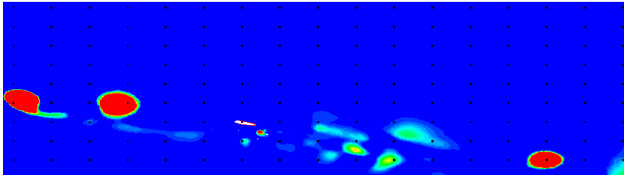
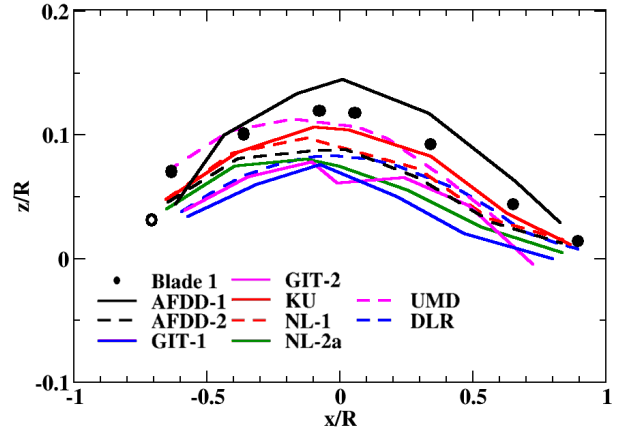
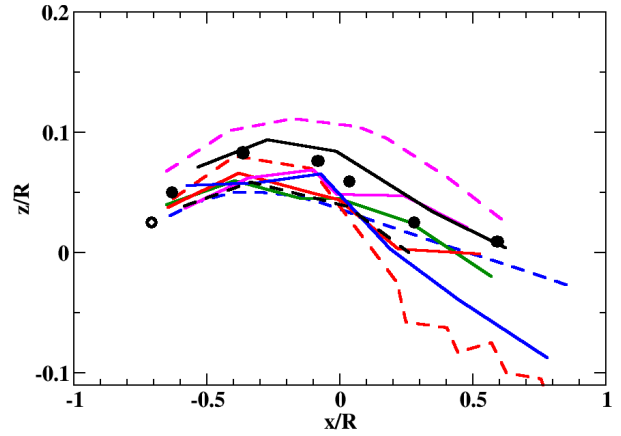


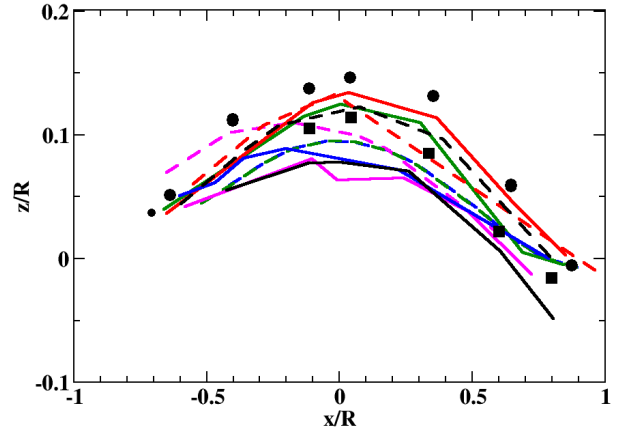
**Fig. 32. Example vorticity plot to locate the tip vortex positions**



(a) Baseline



(b) Minimum noise



(c) Minimum vibration

**Fig. 33. Tip vortex trajectories, advancing side  $y = 0.7R$  (The blade tip location is denoted by the open symbol.)**

hoc method of extracting these values, but overall, the different computational methods predict the values within 5% of the rotor radius (0.1 m). The KU vortices and AFDD-1 vortex tracks are consistently the most accurate of the partners' across all three cases, and this is reflected in the prior observations that these methods provide some of the most consistent results. The NL-1 positions, exclusive of the aft portion of the minimum noise case is also very accurate. The lower position of the vortex track for NL-2 and GIT-1 is not unexpected given the smaller influence of the BVI in the aerodynamic loading (Figs. 13 and 17) through the lower amplitudes of the oscillatory loading.

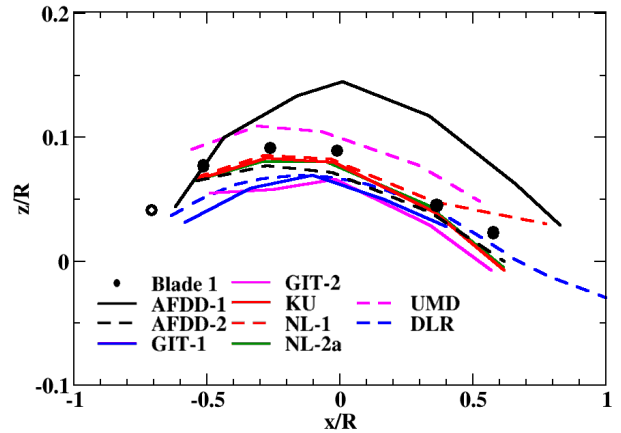
There is a counter-rotating vortex that appears on the advancing side of the MV case, which is indicated in Fig. 33(c) as the second set of filled squares. The counter-rotating vortices were observed in the CFD/CSD simulations, but as only one partner provided that data, the comparisons are not included here.

**Retreating side** The predicted vortex tracks from the simulations are much more accurate on the retreating side (Fig. 34), which is also not unexpected due to the more consistent results observed for the aerodynamic loading (Figs. 14 and 18). Most of the partners results are surprisingly coincident given the method of obtaining the locations. The prescribed wake comprehensive code computations by DLR, show relatively comparable position tracking for both the advancing and retreating sides, indicating that the additional computational effort for CFD/CSD coupling is not necessary for this parameter.

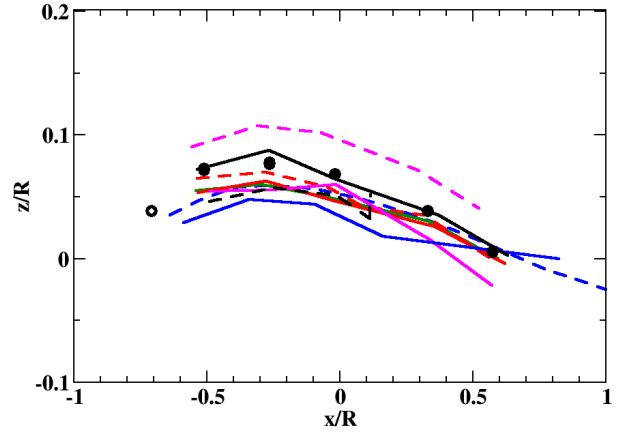
## CONCLUSIONS

There are many factors affecting the accuracy of a CFD/CSD coupled analysis. In most cases, the CFD code has the greatest impact on the quality of the simulations.

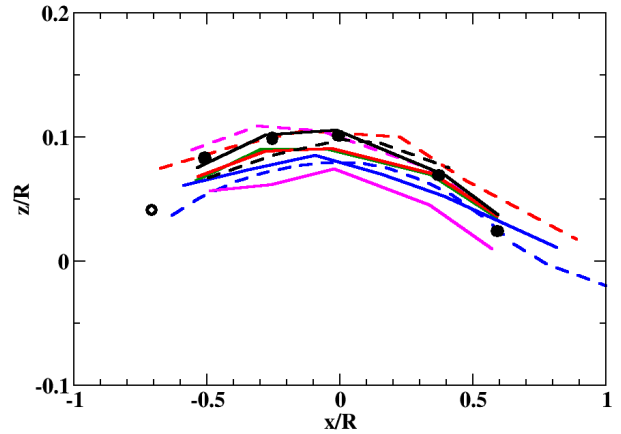
- In the HART II case where the interaction between the blades and their trailed vortices is of major concern, a certain level of higher-order numerical schemes in either the spatial discretization process or the time advancing algorithm is believed to be crucial for enhanced predictions. In addition, the off-body grid spacing, grid refinement techniques, time step size coupled with the number of subiterations, and so on are the important contributors. For a RANS (Reynolds-Averaged Navier-Stokes) calculation, the turbulence model should be properly incorporated in the analysis, but the influence of different turbulence models studied thus far does not appear to have a significant impact on the solution accuracy.
- The full CFD/CSD methods predicted relatively comparable behavior for the normal force and pitching moments using similar turbulence models and temporal



(a) Baseline



(b) Minimum noise



(c) Minimum vibration

**Fig. 34. Tip vortex trajectories, retreating side  $y = -0.7R$  (The blade tip location is denoted by the open symbol.)**

integration. Larger temporal integration, in particular with second-order spatial schemes appear to miss some of the BVI events on the advancing side of the rotor disk. The most accurate correlations paired a two-equation turbulence model with small time steps. Improvements using the same methodology with a detached eddy simulation and smaller time steps were also observed. These are comparable to observations from the UH60A workshop for rotor simulations with dynamic stall (Refs. 68, 69).

- The BVI events associated with the advancing rotor disk are influenced by the fuselage, while the events on the retreating side of the rotor disk are not sensitive to the fuselage. The results from unstructured methods, which currently apply second-order spatial schemes, indicate the need to improve the quality of the grid in this area to capture these events. The advances underway for higher-order discontinuous Galerkin methods for unstructured methods should alleviate some of this, as noted by the improved predictions by the structured methods that apply fourth- to sixth-order spatial schemes. In particular, the baseline HART II case will provide an excellent case to test these new schemes.
- Additional grid refinement (from a nominal engineering quality grid) appears to be less influential than other CFD parameters, such as time step and turbulence modeling.
- Two hybrid methods examined have mixed results in accuracy. These methods over predict some of the characteristics of the BVI in the first quadrant. As this behavior is not observed for the most part by the comprehensive code nor the full CFD/CSD methods, which all include a fuselage model, the less accurate predictions point to the lack of modeling the fuselage. The development of a fuselage model, perhaps similar to that within the S4 comprehensive code, appears to be warranted.
- Computation correlation with experiment for the normal forces is more accurate than pitching moments, as expected. Lead-lag deflections and lag bending moments are accurately predicted by the almost all of the methods, regardless of the different computational methods and options.
- Blade elastic twist predictions, as characterized by the tip deflections, are predicted well by many of the full CFD/CSD methods. This prediction, in concert with accurate predictions of the unsteady flap oscillations, appears to be important for accurate aerodynamic loading at the outboard location where BVI occurs. There appears to be less correlation of the prediction of the vortex locations with the accuracy of these other variables related to BVI.

- The observations associated with the vortex location compared with the rotor elastic deflections and aerodynamic loading suggest that the vortex strength is another parameter of interest that should be studied with CFD/CSD simulations. It is already a parameter evaluated with comprehensive codes, but it has not been examined in detail with CFD/CSD methods. In particular, the dual-vortex pair that is observed with the minimum vibration case has not been examined by most of the partners due to the labor intensive requirements to extract the vortex characteristics from the CFD/CSD flow field.
- Most current CFD/CSD analyses apply an off-body grid spacing of 10% chord length, which is significantly larger than the actual vortex core size as noted during the HART II wind tunnel test. The influence of grid adaptation strategies under development on wake core size is recommended for quantitative evaluation with respect to the accuracy of the variables of interest.
- While the CFD/CSD methods more accurately predict the flap bending moments compared to comprehensive codes (Ref. 2), analysis of predictive capabilities for both the CFD and CSD modules needs further investigation, as no clear consensus exists with the set of CFD/CSD methods evaluated.

## ACKNOWLEDGMENTS

The authors would like to acknowledge the support of HART II partners: DLR, DNW, NASA, Onera, and AFDD. In addition, the authors would like to thank all of their colleagues, students, or advisors for their collaboration:

**AFDD-2:** Andy Wissink, Anubhav Datta, Mark Potsdam, Venke Sankaran, Jay Sitaraman, and Roger Strawn of the Helios development team.

**GIT-1:** Michael Acierno and Nicolas Reveles, Graduate Research Assistants at the Georgia Institute of Technology, and Dr. C. Eric Lynch, a graduate of the Georgia Institute of Technology. Prof. Olivier Bauchau of the Shanghai Jiao Tong University provided insights to permit the modification of DYMORE4 for HHC.

**GIT-2:** Prof. Lakshmi N. Sankar and Dr. Kyle Collins of the Georgia Institute of Technology. Prof. Olivier Bauchau provided DYMORE2.

**KU:** Young-Hyun You and Jeong-Hwan Sa, Graduate Research Assistants at Konkuk University.

**NASA-LaRC:** Elizabeth M. Lee-Rausch of the NASA Langley Computational AeroSciences Branch for generating the unstructured computational meshes used for the FUN3D simulations.



UM: Mathieu Amiraux and Sebastian Thomas, Graduate Research Assistants at University of Maryland.

## References

- <sup>1</sup>van der Wall, B. G., "A Comprehensive Rotary-Wing Database for Code Validation: The HART II International Workshop," *The Aeronautical Journal of the Royal Aeronautical Society*, Vol. 115, No. 1163, January 2011, pp. 91–102; erratum in Vol. 115, No. 1166, April 2011, p. 220.
- <sup>2</sup>van der Wall, B. G., Lim, J., Smith, M.J., Jung, S. N., Bailly, J., Amiraux, M., and Boyd, D. D., Jr., "An Assessment of Comprehensive Code Prediction State-of-the-Art Using the HART II International Workshop Data," *Proceedings of the 68th American Helicopter Society Forum*, Ft. Worth, TX, May 1–3, 2012.
- <sup>3</sup>van der Wall, B.G., Burley, C.L., Yu, Y.H., Pengel, K., Beaumier, P., "The HART II Test - Measurement of Helicopter Rotor Wakes," *Aerospace Science and Technology*, Vol. 8, No. 4, June 2004, pp. 273–284.
- <sup>4</sup>van der Wall, B.G., "2nd HHC Aeroacoustic Rotor Test (HART II) - Part I: Test Documentation," DLR-IB 111-2003/31, German Aerospace Center (DLR), 2003.
- <sup>5</sup>van der Wall, B.G., Burley, C.L., "2nd HHC Aeroacoustic Rotor Test (HART II) - Part II: Representative Results," DLR-IB 111-2005/03, German Aerospace Center (DLR), 2005.
- <sup>6</sup>Schneider, O., "Analysis of SPR Measurements of HART II," *Aerospace Science and Technology*, Vol. 9, No. 5, July 2005, pp. 409–420.
- <sup>7</sup>Lim, J. W., Tung, C., Yu, Y. H., Burley, C. L., Brooks, T. F., Boyd, D., van der Wall, B. G., Schneider, O., Richard, H., Raffel, M., Beaumier, P., Delrieux, Y., Pengel, K., and Mercker, E., "HART II: Prediction of Blade-Vortex Interaction Loading," *Proceedings of the 29th European Rotorcraft Forum*, Friedrichshafen, Germany, September 2003.
- <sup>8</sup>Anderson, W. K. and Bonhaus, D. L., "An Implicit Upwind Algorithm for Computing Turbulent Flows on Unstructured Grids," *Computers and Fluids*, Vol. 23, No. 1, January 1994, pp. 1–22.
- <sup>9</sup>"<http://fun3d.larc.nasa.gov>, Last accessed December 15, 2011."
- <sup>10</sup>Biedron, R. T. and Thomas, J. L., "Recent Enhancements to the FUN3D Flow Solver for Moving Mesh Applications," AIAA-2009-1360, 47th AIAA Aerospace Sciences Meeting, Orlando, FL, January 2009.
- <sup>11</sup>Vatsa, V. N., Carpenter, M. H., and Lockard, D. P., "Re-evaluation of an Optimized Second Order Backward Difference (BDF2OPT) Scheme for Unsteady Flow Applications," AIAA-2010-0122, 48th AIAA Aerospace Sciences Meeting, Orlando, FL, January 2010.
- <sup>12</sup>Vatsa, V. and Carpenter, M. H., "Higher-Order Temporal Schemes with Error Controllers for Unsteady Navier-Stokes Equations," AIAA-2005-5245, 17th AIAA Computational Fluid Dynamics Conference, Toronto, ON, Canada, June 2005.
- <sup>13</sup>Noack, R. W., "DiRTlib: A Library to Add an Overset Capability to Your Flow Solver," AIAA -2005-5116, 17th AIAA Computational Fluid Dynamics Conference, Toronto, Canada, June 2005.
- <sup>14</sup>Noack, R. W., Bogar, D. A., Kunz, R. F., and Carrica, P. M., "SUGGAR++: An Improved General Overset Grid Assembly Capability," AIAA-2009-3992, 19th AIAA Computational Fluid Dynamics Conference, San Antonio, TX, June 2009.
- <sup>15</sup>O'Brien, D.M., Jr., *Analysis of Computational Modeling Techniques for Complete Rotorcraft Configurations*, Ph.D. Dissertation, School of Aerospace Engineering, Georgia Institute of Technology, Atlanta, GA, May 2006.
- <sup>16</sup>Biedron, R. T. and Lee-Rausch, E. M., "Rotor Airloads Prediction Using Unstructured Meshes and Loose CFD/CSD Coupling," AIAA-2008-7341, 26th AIAA Applied Aerodynamics Conference, Honolulu, HI, August 2008.
- <sup>17</sup>Johnson, W., "Rotorcraft Aerodynamics Models for a Comprehensive Analysis," *Proceedings of the American Helicopter Society 54th Annual Forum*, Washington, D.C., May 20–22, 1998.
- <sup>18</sup>Abras, J.N., *Enhancement of Aeroelastic Rotor Airloads Prediction Methods*, Ph.D. Dissertation, School of Aerospace Engineering, Georgia Institute of Technology, Atlanta, GA, May 2009.
- <sup>19</sup>Reveles, N., Smith, M. J., Zaki, A., and Bauchau, O.A., "A Kriging-Based Trim Algorithm For Rotor Aeroelasticity," *Proceedings of the 37th European Rotorcraft Forum*, Gallarate, Italy, September 12–15, 2011.
- <sup>20</sup>Bauchau, O.A., Bottasso, C.L., Nikishkov, Y.G., "Modeling Rotorcraft Dynamics with Finite Element Multibody Procedures," *Mathematical and Computer Modeling*, Vol. 33, Vol. 10-11, May–June 2001, pp. 1113–1137.
- <sup>21</sup>Potsdam, M., Yeo, H., and Johnson, W., "Rotor Airloads Prediction Using Loose Aerodynamic/Structural Coupling," *AIAA Journal of Aircraft*, Vol. 43, No. 3, May–June 2006, pp. 732–742.

- <sup>22</sup>Min, B. Y., *A Physics Based Investigation of Gurney Flaps for Enhancement of Rotorcraft Flight Characteristics*, Ph. D. Dissertation, School of Aerospace Engineering, Georgia Institute of Technology, Atlanta, GA, May 2010.
- <sup>23</sup>Min, B. Y., and Sankar, L. N., "Hybrid Navier-Stokes/Free Wake Method for Modeling Blade Vortex Interactions," *Journal of Aircraft*, Vol. 47, No. 3, May–June 2010, pp. 975–982.
- <sup>24</sup>Sankaran, V., Wissink, A., Datta, A., Sitaraman, J., Jayaraman, B., Potsdam, M., Kamkar, S., Katz, A., Mavriplis, D., Saber, H., Roget, B., and Strawn, R., "Overview of the Helios V2.0 Computational Platform for Rotorcraft Simulations," AIAA-2011-1105, 49th Aerospace Sciences Meeting and Exhibit, Orlando, FL, January 4–7, 2011.
- <sup>25</sup>Wissink, W., Sankaran, V., Datta, A., Jayaraman, B., Potsdam, M., Kamkar, S., Sitaraman, J., Mavriplis, D., Strawn, R., "Capability Enhancements Version 3 of the Helios High-Fidelity Rotorcraft Simulation Code," AIAA Paper 2012-0713, 50th Aerospace Sciences Meeting and Exhibit, Nashville, TN, January 9–12, 2012.
- <sup>26</sup>Saber, H., Khoshlahjeh, M., Ormiston, R., and Rutkowski, M. J., "Overview of RCAS and Application to Advanced Rotorcraft Problems," Proceedings of the 4th AHS Decennial Specialist's Conference on Aeromechanics, San Francisco, CA, January 21–23, 2004.
- <sup>27</sup>Kim, J. W., Park, S. H., and Yu, Y. H., "Euler and Navier-Stokes Simulations of Helicopter Rotor Blade in Forward Flight Using an Overlapped Grid Solver," AIAA-2009-4268, 19th AIAA CFD Conference, San Antonio, TX, June 2009.
- <sup>28</sup>Cho, K. W., Kwon J. H., and Lee, S., "Development of a Fully Systemized Chimera Methodology for Steady/Unsteady Problems," *Journal of Aircraft*, Vol. 36, No. 6, November–December 1999, pp. 973–980.
- <sup>29</sup>van der Wall, B. G., "Mode Identification and Data Synthesis of HART II Blade Deflection Data," Institute Report, IB 111-2007/28, German Aerospace Center (DLR), 2007.
- <sup>30</sup>Chan, W., Meakin, R., and Potsdam, M., "CHSSI Software for Geometrically Complex Unsteady Aerodynamic Applications," AIAA Paper 2001-0593, 15th AIAA Computational Fluid Dynamics Conference, Anaheim, CA, June 11–14, 2001.
- <sup>31</sup>Lim, J. W., Nygaard, T. A., Strawn, R., and Potsdam, M., "Blade-Vortex Interaction Airloads Prediction Using Coupled Computational Fluid and Structural Dynamics," *Journal of the American Helicopter Society*, Vol. 52, No. 4, 2007, pp. 318–328.
- <sup>32</sup>Lim, J., and Strawn, R., "Computational Modeling of HART II Blade-Vortex Interaction Loading and Wake System," *Journal of Aircraft*, Vol. 45, No. 3, May–June 2008, pp. 923–933.
- <sup>33</sup>Sitaraman, J., Baeder, J., and Chopra, I., "Validation of UH-60 Rotor Blade Aerodynamic Characteristics Using CFD," Proceedings of the 59th Annual Forum of the American Helicopter Society International, Phoenix, AZ, May 6–8, 2003.
- <sup>34</sup>Yoon, S., and Jameson, A., "Lower-Upper Symmetric-Gauss-Seidel Method for Euler and Navier-Stokes Equations," *AIAA Journal*, Vol. 26, No. 9, 1988, pp. 1025–1026.
- <sup>35</sup>Pulliam, T., "Time Accuracy and the Use of Implicit Methods," AIAA-1993-3360, AIAA 11th Computational Fluid Dynamics Conference, Orlando, FL, July 6–9, 1993.
- <sup>36</sup>Gopalan, G., Sitaraman, J., Baeder, J. D. and Schmitz, F. H., "Aerodynamic and Aeroacoustic Prediction Methodologies with Application to the HART II Model Rotor," Presented at the 62nd Forum of the American Helicopter Society, Phoenix, AZ, May 9–11, 2006.
- <sup>37</sup>Leishman, J. G., Bhagwat, M. J. and Ananthan, S., "Free-Vortex Wake Predictions of the Vortex Ring State for Single-Rotor and Multi-Rotor Configurations," Proceedings of the American Helicopter Society 58th Annual Forum, Montreal, Canada, June 11–13, 2002.
- <sup>38</sup>Bhagwat, M. J., Leishman, J. G., "Generalized Viscous Vortex Model for Application to Free-Vortex Wake and Aeroacoustic Calculations," Proceedings of the American Helicopter Society 58th Annual Forum, Montreal, Canada, June 11–13, 2002.
- <sup>39</sup>Datta, A., *Understanding, Prediction and Validation of Rotor Vibratory Loads in Steady Level Flight*, Doctoral Dissertation, University of Maryland, College Park, MD, 2004.
- <sup>40</sup>Peters, D.A. and Barwey, D., "A General Theory of Rotorcraft Trim," *Mathematical Problems in Engineering*, Vol. 2, No. 1, Jan. 1996, pp. 1–34.
- <sup>41</sup>Zaki, A., *Using Tightly-Coupled CFD/CSD Simulation for Rotorcraft Stability Analysis*, PhD Thesis, Georgia Institute of Technology, Atlanta, Georgia, January 2012.
- <sup>42</sup>van der Wall, B.G., "Analytic Formulation of Unsteady Profile Aerodynamics and its Application to Simulation of Rotors," ESA-TT-1244, German Aerospace Center, 1992 (Translation of the Research Report DLR-FB 90-28, 1990).
- <sup>43</sup>von Grünhagen, W., "Bestimmung der gekoppelten Schlagbiede-, Schwenkbiede- und Torsionsschwingungen für beliebige Rotorblätter mit Hilfe der Finite-Element-Methode (Computation of the Coupled Flap Bending,

Lag Bending and Torsion Oscillations for Arbitrary Rotor Blades with the Aid of the Finite Element Method),” DFVLR IB 154-80/21, German Aerospace Center, 1980.

<sup>44</sup>Houbold, J.C., and Brooks, G.W., “Differential Equations of Motion for Combined Flapwise Bending, Chordwise Bending, and Torsion of Twisted Nonuniform Rotor Blades,” NACA TN 3905, 1957.

<sup>45</sup>Leiss, U., “A Consistent Mathematical Model to Simulate Steady and Unsteady Rotor-Blade Aerodynamics,” Proceedings of the 10th European Rotorcraft Forum, The Hague, Netherlands, Aug. 28–31, 1984.

<sup>46</sup>van der Wall, B.G., Göpel, C., “Über den Einfluss der Rotorversuchsstände ROTEST und ROTOS auf die Rotor durchströmung im DNW (About the Influence of the Rotor Test Rigs ROTEST and ROTOS to the Airflow in the Rotor Disk in the DNW),” DLR-Mitteilung 91-16, German Aerospace Center, 1991.

<sup>47</sup>Beddoes, T.S., “A Wake Model for High Resolution Airloads,” AHS/ARO 1st International Conference on Rotorcraft Basic Research, Research Triangle Park, NC, USA, Feb. 19-21, 1985.

<sup>48</sup>van der Wall, B.G., “Extensions of Prescribed Wake Modeling for Helicopter Rotor BVI Noise Investigations,” *CEAS Aeronautical Journal*, accepted, DOI 10.1007/s13272-012-0045-9, 2012.

<sup>49</sup>Chopra, I., and Bir, G., “University of Maryland Advanced Rotor Code: UMARC,” American Helicopter Society Aeromechanics Specialists Conference, San Francisco, CA, USA, Jan. 19–21, 1994.

<sup>50</sup>Hodges, D.H., and Dowell, E.H., “Nonlinear Equations of Motion for the Elastic Bending and Torsion of Twisted Nonuniform Rotor Blades,” NASA TN D-7818, 1974.

<sup>51</sup>Hodges, D.H., Ormiston, R.A., and Peters, D.A., “On the Nonlinear Deformation Geometry of Euler-Bernoulli Beams,” NASA TP 1566, 1980.

<sup>52</sup>Lim, J. W., and Dimanlig, A. C. B., “The Effect of Fuselage and Rotor Hub on Blade-Vortex Interaction Airloads and Rotor Wakes,” Proceedings of the 36th European Rotorcraft Forum, Paris, France, September 7–9, 2010.

<sup>53</sup>Lim, J. W., Wissink, A., Jayaraman, B., and Dimanlig, A., “Helios Adaptive Mesh Refinement for HART II Rotor Wake Simulations,” Proceedings of the 48th American Helicopter Society Annual Forum, Ft. Worth, TX, May 1–3, 2012.

<sup>54</sup>Jayaraman, B., Wissink, A., Lim, J., Potsdam, M., and Dimanlig, A., “Helios Prediction of Blade-Vortex Interaction and Wake of the HART II Rotor,” AIAA-2012-0714, 50th Aerospace Sciences Meeting and Exhibit, Nashville, TN, January 9–12, 2012.

<sup>55</sup>Boyd, D.D., Jr., “HART II Acoustic Predictions Using a Coupled CFD/CSD Method,” Proceedings of the American Helicopter Society 65th Annual Forum, Grapevine, TX, May 2009.

<sup>56</sup>Boyd, D.D., Jr., “Initial Aerodynamic and Acoustics Study of an Active Twist Rotor Using a Loosely Coupled CFD/CSD Method,” Proceedings of the 35th European Rotorcraft Forum, Hamburg, Germany, September 2009.

<sup>57</sup>Pirzadeh, S., “Three-Dimensional Unstructured Viscous Grids by the Advancing Front Method,” *AIAA Journal*, Vol. 34, No. 1, January 1996, pp. 43–49.

<sup>58</sup>Roe, P. L., “Approximate Riemann Solvers, Parameter Vectors, and Difference Schemes,” *Journal of Computational Physics*, Vol. 43, October 1981, pp. 357–372.

<sup>59</sup>Spalart, P. R. and Allmaras, S. R., “A One-Equation Turbulence Model for Aerodynamic Flows,” *La Recherche Aeronautique*, No. 1, 1994, pp. 5–21.

<sup>60</sup>Park, S. H., and Kwon, J. H., “Implementation of  $k-\omega$  Turbulence Models in an Implicit Multigrid Method,” *AIAA Journal*, Vol. 42, No. 7, 2004, pp. 1348–1357.

<sup>61</sup>Furchert, R., “Bestimmung der Eigenfrequenzen und Eigenformenvon 3 Rotorblattsätzen des Rotorversuchsstands, (Determination of Natural Frequencies and Modes of 3 Rotor Blade Sets of the Rotor Test Rig),” IB 111-92/11, German Aerospace Center, 1992.

<sup>62</sup>Bousman, W. G., “Putting the Aero Back in Aeroelasticity,” NASA/TM-2000-209589, USAAMCOM-TR-00-A-005, March 2000.

<sup>63</sup>Bousman, W.G., and Norman, T., “Assessment of Predictive Capability of Aeromechanics,” *Journal of the American Helicopter Society*, Vol. 55 No. 1, January 2010, pp. 012001/1-12.

<sup>64</sup>Heyson, H.H., “Use of Superposition in Digital Computers to Obtain Wind Tunnel Interference Factors for Arbitrary Configurations, With Particular Reference to V/STOL Models,” NASA TR R-302, 1969.

<sup>65</sup>Langer, H.-J., “An Experimental Evaluation of Wind Tunnel Wall Correction Methods for Helicopter Performance,” Proceedings of the 52nd Annual Forum of the American Helicopter Society, Washington, DC, June 4–6, 1996.

<sup>66</sup>Moulton, M. and Smith, M. J., “The Prediction and Validation of Static and Dynamic Stall,” Proceedings of the AHS International Meeting on Advanced Rotorcraft Technology and Safety Operations, Ohmiya, Japan, November 1–3, 2010.

<sup>67</sup>Biedron, R., and Lee-Rausch, E., “An Examination of Unsteady Airloads on a UH-60A Rotor: Computation vs. Measurement,” Proceedings of the 68th American Helicopter Society Forum, Ft. Worth, TX, May 1–3 2012.

<sup>68</sup>Abras, J., Lynch, C. E., and Smith, M., “Rotorcraft Methodology For Unstructured CFD-CSD Coupling,” *Journal of the American Helicopter Society*, Vol. 57 (1), pp. 1–14, Jan, 2012, doi: 10.4050/JAHS.57.01200.

<sup>69</sup>Bousman, W. G., “UH60A Workshop CFD/CSD Comparison Book 5,” unpublished.

<sup>70</sup>van der Wall, B.G., “Mode Identification and Data Synthesis of HART II Blade Deflection Data,” DLR-IB 111-2007/28, German Aerospace Center, 2007.

**Table 7. Baseline Computation Mean Values**

	Aerodynamic Loads		Structural Moments			Tip Deflections		
	Normal Force ( $C_n M^2$ )	Pitching Moment ( $C_m M^2$ )	Flap (Nm)	Lag (Nm)	Torsion (Nm)	Flap ( $100z_{el}/R$ )	Lead-Lag ( $100x_{el}/R$ )	Elastic Twist ( $^\circ$ )
Experiment	0.0902	-0.0026	-9.27	-10.55	-10.55	-0.871	-0.917	-0.917
AFDD-1	0.0775	-0.0039	3.87	51.67	-0.01	-0.914	-1.894	-1.894
AFDD-2	0.0766	-0.0032	2.56	47.04	-7.85	-0.955	-1.438	-1.438
GIT-1	0.0723	-0.0035	-3.14	0.00	-4.49	-0.939	-1.995	-1.995
GIT-2	0.0787	-0.0046	-1.61	56.78	-5.69	-0.997	-2.384	-2.384
KU	0.0800	-0.0027	-0.84	-9.94	-3.49	-0.879	-1.232	-1.232
NL-1	0.0782	-0.0040	3.19	57.21	48.36	-0.915	-1.922	-1.922
NL-2a	0.0820	-0.0029	3.41	58.12	-3.62	-0.777	-1.151	-1.151
NL-2b	0.0814	-0.0030	3.52	58.12	-3.71	-0.778	-1.167	-1.167
UMD	0.0892	-0.0025	-13.62	-2.94	-2.94	-0.657	-1.204	-1.204
DLR	0.0863	-0.0027	-12.48	15.02	-1.31	-1.036	-0.724	-0.724

**Table 8. Minimum Noise Computation Mean Values**

	Aerodynamic Loads		Structural Moments			Tip Deflections		
	Normal Force ( $C_n M^2$ )	Pitching Moment ( $C_m M^2$ )	Flap (Nm)	Lag (Nm)	Torsion (Nm)	Flap ( $100z_{el}/R$ )	Lead-Lag ( $100x_{el}/R$ )	Elastic Twist ( $^\circ$ )
Exp.	0.0878	-0.0058	-8.925	-9.761	-2.885	-0.65	1.37	-0.61
AFDD-1	0.0768	-0.0040	3.875	54.248	0.080	-0.91	-0.62	-1.82
AFDD-2	0.0755	-0.0033	2.088	23.230	-1.281	-0.98	0.59	-1.28
GIT-1	0.0743	0.0000	-3.151	0.000	-4.569	-0.99	-0.16	-1.94
GIT-2	0.0822	-0.0046	-1.261	58.353	-5.641	-0.91	0.71	-2.36
KU	0.0812	-0.0030	-0.718	-12.981	-3.448	-0.87	-0.36	-1.13
NL-1	0.0767	-0.0042	3.398	51.121	-4.748	-0.93	-0.43	-1.89
NL-2a	0.0809	-0.0030	3.629	61.083	-3.691	-0.79	-0.28	-1.17
NL-2b	0.0802	-0.0031	3.496	61.351	-3.805	-0.80	-0.28	-1.20
UMD	0.0921	-0.0025	0.000	0.027	0.000	-0.64	-0.24	-1.17
DLR	0.1009	-0.0026	-12.630	18.420	-1.180	-0.96	0.23	-0.83

**Table 9. Minimum Vibration Computation Mean Values**

	Aerodynamic Loads		Structural Moments			Tip Deflections		
	Normal Force ( $C_n M^2$ )	Pitching Moment ( $C_m M^2$ )	Flap (Nm)	Lag (Nm)	Torsion (Nm)	Flap ( $100z_{el}/R$ )	Lead-Lag ( $100x_{el}/R$ )	Elastic Twist ( $^\circ$ )
Exp.	0.1025	-0.0051	-8.785	-9.887	-2.916	-0.48	1.39	-0.75
AFDD-1	0.0761	-0.0040	3.322	52.593	-0.022	-0.97	-0.67	-1.97
AFDD-2	0.0787	-0.0029	0.673	22.844	-7.827	-0.95	0.67	-1.32
GIT-1	0.0710	-0.0046	-3.084	0.000	-4.564	-1.03	-0.21	-1.95
GIT-2	0.0774	-0.0046	-1.863	56.906	-5.672	-1.04	-0.66	-2.37
KU	0.0792	-0.0031	-1.026	-9.722	-3.527	-0.86	0.36	-1.33
NL-1	0.0770	-0.0041	3.020	48.793	-4.885	-0.93	-0.45	-2.01
NL-2a	0.0801	-0.0030	3.296	58.345	-3.755	-0.82	-0.30	-1.20
NL-2b	0.0797	-0.0031	3.363	58.961	-3.853	-0.82	-0.30	-1.23
UMD	0.0901	-0.0025	-13.355	19.982	-3.456	-0.63	-0.24	-1.18
DLR	0.0884	-0.0026	-12.150	15.410	-1.270	-1.04	0.20	-0.89